Macromolecules

pubs.acs.org/Macromolecules Article

Expanding the Scope of Self-Assembly: Heat-Induced Self-Assembly of Block Copolymers with High Solids

Jingwei Zhang, Boyang Shi, Xiaoxiao Wu, Xiaotong Fang, Xinyue Liang, Zhou Peng, and Guowei Wang*

Cite This: *Macromolecules* 2025, 58, 4985−5000 Read Online

ACCESS | Metrics & More | Article Recommendations | Supporting Information

ABSTRACT: Polymerization-induced self-assembly (PISA) has gained widespread recognition as a potent tool for accessing nano-objects with diverse morphologies. To facilitate its practical application, further development of the self-assembly method is still urgent and challenging. We herein report an innovative self-assembly approach termed heat-induced self-assembly (HISA), enabling the preparation of nano-objects with abundant morphologies by direct thermal dissolution of solid block copolymers (BCPs) in selective solvents at elevated concentration (20% w/w). The BCPs of polyisoprene-*b*-polystyrene (PI-*b*-PS), polyisoprene-*b*-poly(methyl methacrylate) (PI-*b*-PMMA), and polyisoprene-*b*-poly(4-vinylpyridine) (PI-*b*-P4VP) were prepared by living anionic polymerization (LAP) for HISA investigation. Furthermore, this methodology was extended to heat-induced cooperative assembly (HICA) comprising PI-*b*-PS$_m$/PS$_n$ (AB$_m$/B$_n$) and PI-*b*-PS$_m$/PI-*b*-PS$_n$ (AB$_m$/AB$_n$), where B represented the PS core-forming block. The feasibility of HISA and HICA processes was investigated, and a library of morphologies, including spheres, worms, vesicles, nanotubes, and sponges, were collected. The pseudophase diagrams were constructed for both AB$_m$/B$_n$ and AB$_m$/AB$_n$ systems to provide guiding principles for the tailored morphologies. To evaluate the universality of HISA and HICA techniques, the AC$_m$/C$_n$ and AB$_m$/AC$_n$ systems (C represented PMMA or P4VP core-forming block) were further investigated. The corresponding glass transition temperatures (T_gs) of BCPs in both dry and solvated states were analyzed to gain further insights into the HISA and HICA techniques. These high-concentration assembly strategies including HISA and HICA combined operational simplicity with morphological diversity, showing significant potential in practical applications.

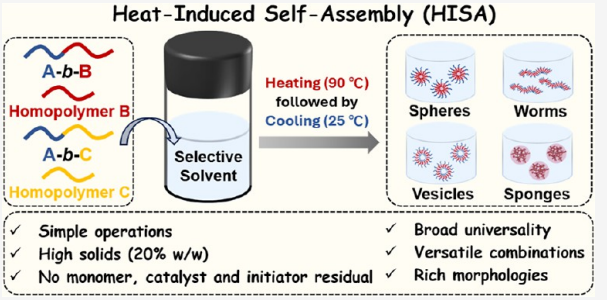

INTRODUCTION

The self-assembly of amphiphilic block copolymers (BCPs) has generated nano-objects with diverse morphologies, demonstrating unique applications across multiple fields.[1−4] Early methods for obtaining nano-objects involved self-assembly of amphiphilic BCPs in a selective solvent. Nevertheless, this method suffered from acknowledged shortcomings such as time-demanding dialysis and low copolymer concentrations (<1.0% w/w).[5,6] In contrast, polymerization-induced self-assembly (PISA) has emerged as a transformative approach that enables simultaneous polymerization and in situ self-assembly through one-pot synthesis, particularly at high concentrations (up to 50% w/w).[7−9]

Typically, the PISA process starts from a macroinitiator/stabilizer, which can be well solubilized in a mixture of a selected solvent and the second monomer. Through the controlled/"living" polymerization mechanisms, the core-forming block can be generated, and the solubility was gradually decreased. This resulted in self-assembly of BCPs, and a broad spectrum of well-defined nano-objects was obtained in a dispersion system.[10−12] Based on the above prototype, the PISA technique has been extensively derived and updated in recent years, aiming to simplify the operations, enrich the morphologies, and facilitate the applications. For example, to diversify the compositions of nano-objects, the nitroxide-mediated radical polymerization (NMRP),[13−15] reversible addition−fragmentation chain transfer (RAFT) polymerization,[10,16−18] atom transfer radical polymerization (ATRP),[19−21] ring-opening metathesis polymerization (ROMP),[22−24] and living anionic polymerization (LAP)[25−27] mechanisms have been introduced into the PISA process. To enrich the morphological evolution window, the cooperative self-assembly strategy was derived and the polymerization-induced cooperative self-assembly (PICA) process was developed, effectively accelerating morphological transitions toward higher-order morphologies.[28−31] To simplify the operations, some PISA formulations were optimized and performed in a one-pot manner,[10,11,32] and some self-assembly processes were also conversely realized from core-forming block to stabilizer block by overturning the conventional

Received: November 14, 2024
Revised: April 4, 2025
Accepted: April 14, 2025
Published: April 18, 2025

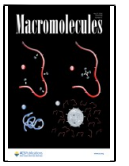

https://doi.org/10.1021/acs.macromol.4c02808
Macromolecules 2025, 58, 4985−5000

Scheme 1. (a) Synthesis of PI-*b*-PS, PI-*b*-PMMA, and PI-*b*-P4VP by the LAP Process. (b) Illustration of the HISA or HICA Process for PI-*b*-PS, PI-*b*-PS$_m$/PS$_n$, PI-*b*-PS$_m$/PI-*b*-PS$_n$, PI-*b*-PS$_m$/PI-*b*-PMMA$_n$, and PI-*b*-PS$_m$/PI-*b*-P4VP$_n$ Performed at 90 °C in *n*-Heptane

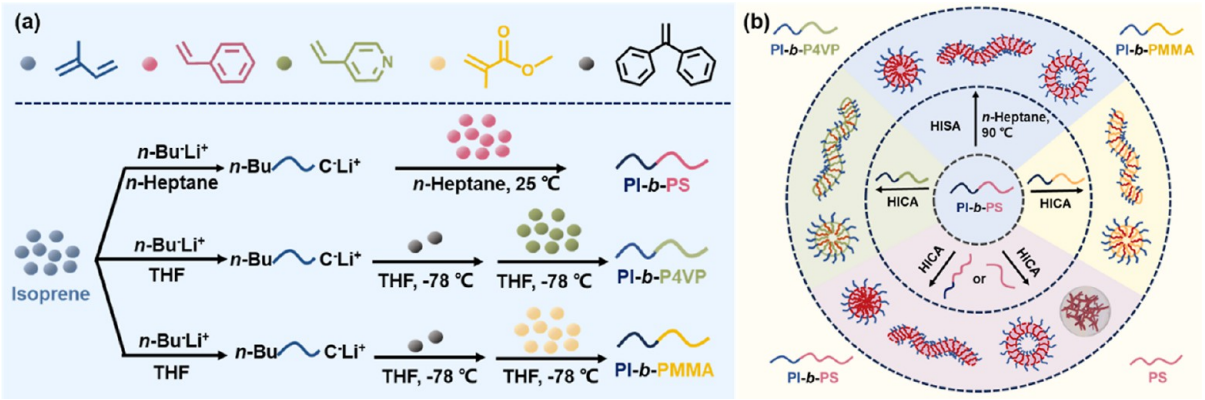

sequence from stabilizer block to core-forming block.[33−37] To improve the functionality, the thermally responsive block was introduced, and the intelligent behavior of nano-objects could be elaborately modulated by temperature.[17,32,38−40] Despite the remarkable development and widespread recognition of the PISA process as a powerful approach for fabricating nano-objects with controllable sizes, morphologies, and responsiveness, further optimization of this technique remains crucial for enhancing its versatility and practical applications.[10,41] For example, the colors inherited from the RAFT agent in RAFT PISA[42] and the residual metal catalysts in ATRP PISA,[43,44] as well as the remaining low active monomers, might contaminate the nano-objects.[16,45,46] Multicomponent nano-objects for advanced functionalities necessitated laborious synthetic processes.[47,48] The requirement for specialized laboratory infrastructure in controlled/"living" polymerization-based PISA technology created practical constraints. Specifically, the inherent need to store and transport nano-objects in selective solvents substantially elevated operational costs related to logistics, long-term preservation, and safety management. Alternatively, the on-site production of nano-objects from the self-assembled BCPs could be of greater practical significance. As a consequence, these challenges motivate our development of an alternative self-assembly method to overcome the current PISA constraints.

Generally, the self-assembly process relies on the solubility of blocks in selective solvents. Notably, most polymers exhibit temperature-dependent solubility governed by upper critical solution temperature (UCST) or lower critical solution temperature (LCST) behavior.[49−51] In UCST-type systems, exceeding specific temperature thresholds induces dissolution of target blocks in selective solvents, while subsequent cooling below these temperatures drives spontaneous assembly through solubility reduction. Inspired by this thermoresponsive behavior, we hypothesize that thermal energy input might promote BCP chains' plasticization in selective solvents to facilitate assembly processes. In fact, early in 1991, Stejskal et al. had reported the formation of metastable micelles (<1.0% w/w, 20 °C) through direct dissolution of polystyrene-*b*-poly(ethylene-*co*-propylene) (PS-*b*-PEP) in selective solvents (decane for PEP block or dioxane for PS block).[52,53] These metastable structures would further transform into equilibrium spherical micelles once the temperature is raised enough (60 °C) or the core is swollen by a good solvent. Armes et al. adopted a similar strategy to gain further insights into the formation mechanism of well-defined micelles during a thermal cycle (1.0% w/w, 20−110 °C) of PS-*b*-PEP.[54] They elaborated that hot *n*-alkane solvents could cause swelling, known as the partial plasticization of the micellar core. This led to a lower effective glass transition temperature (T_g) for the core-forming PS block and, thus, promoted the self-assembly of BCPs. Despite these seminal advances in thermal-driven assembly, some shortcomings need to be further optimized, such as low copolymer concentration (<1.0% w/w), restricted morphologies (spheres and worms), and limited polymer systems available in this approach. These constraints underscore the necessity for developing next-generation thermal assembly methodologies.

Building upon these foundations, we proposed a facile method termed heat-induced self-assembly (HISA). By subjecting the solid BCPs to a simple heating−cooling cycle in selective solvents (20% w/w), the self-assembly of BCPs could be realized. Furthermore, when the BCPs were combined with homopolymer (AB$_m$/B$_n$) or binary copolymer blends (AB$_m$/AB$_n$ or AB$_m$/AC$_n$), the heat-induced cooperative assembly (HICA) could be performed, which readily generated nano-objects with multiple core-forming blocks. Specifically, a series of polyisoprene-*b*-polystyrene (PI-*b*-PS), polyisoprene-*b*-poly(methyl methacrylate) (PI-*b*-PMMA), and polyisoprene-*b*-poly(4-vinylpyridine) (PI-*b*-P4VP) diblock copolymers were prepared by living anionic polymerization (LAP) and used for the HISA or HICA process in this contribution (Scheme 1a). First, the feasibility of the HISA process was investigated using PI-*b*-PS as the research model, and the morphologies of the identical BCPs obtained by HISA and LAP PISA were compared. Then, motivated by the interest in the efficient access to higher-order morphologies by adding the homopolymer,[26,28,31,55−57] the HICA process of PI-*b*-PS$_m$/PS$_n$ blends was investigated. Similarly, binary copolymer blends of two BCPs (PI-*b*-PS$_m$/PI-*b*-PS$_n$) differing only in the length of the core-forming block were also adopted in the HICA process. The morphologies such as spheres, worms, vesicles, and sponges were captured and systematically characterized by transmission electron microscopy (TEM) and dynamic light scattering (DLS). The pseudophase diagrams of the AB$_m$/B$_n$ system and AB$_m$/AB$_n$ system were constructed to provide guiding principles for the tailored morphologies. Furthermore, the universality of this self-assembly method was evaluated by

https://doi.org/10.1021/acs.macromol.4c02808
Macromolecules 2025, 58, 4985−5000

Table 1. Formulation and Characterization for PI-*b*-PS, PI-*b*-PMMA, and PI-*b*-P4VP BCPs with Varying $DP_{X\ (X=PS/PMMA/P4VP)}$ [a]

		the first block		the second block		
entry	sample[b]	M_n[c]	M_w/M_n[c]	M_n[c]	M_w/M_n[c]	MW ratio $M_{n,PI}/M_{n,X\ (X=PS/PMMA/P4VP)}$[d]
1	PI_{89}-*b*-PS_{117}	6100	1.07	21,000	1.03	1/2
2	PI_{95}-*b*-PS_{168}	6500	1.09	26,000	1.04	1/2.7
3	PI_{82}-*b*-PS_{183}	5600	1.07	30,000	1.05	1/3.4
4	PI_{92}-*b*-PS_{363}	6300	1.06	46,000	1.07	1/6
5	PI_{84}-*b*-PS_{548}	5700	1.07	74,000	1.07	1/10
6	PI_{81}-*b*-$PMMA_{82}$	5500	1.07	11,000	1.08	1/1.5
7	PI_{85}-*b*-$PMMA_{134}$	5800	1.07	18,000	1.06	1/2.3
8	PI_{94}-*b*-$PMMA_{256}$	6400	1.09	27,000	1.11	1/4
9	PI_{77}-*b*-$P4VP_{50}$	5200	1.09	13,000	1.09	1/1
10	PI_{78}-*b*-$P4VP_{101}$	5300	1.07	20,000	1.13	1/2
11	PI_{89}-*b*-$P4VP_{151}$	6100	1.06	29,000	1.16	1/2.6

[a]The PI-*b*-PS BCPs (Entries 1−5) were prepared in *n*-heptane with solids content of 20% w/w by the LAP PISA process. PI-*b*-PMMA (Entries 6−8) and PI-*b*-P4VP BCPs (Entries 9−11) were prepared in THF by the LAP process. [b]The subscripts represented the DP of each block, which was calculated according to the SEC results (DP_{PI}) and ^{1}H NMR spectra ($DP_{X\ (X=PS/PMMA/P4VP)}$). [c]The M_n and M_w/M_n were obtained by SEC measurement using THF as eluent and PS as the standard (Entries 1−5), THF as eluent and PMMA as the standard (Entry 6−8), and DMF as eluent and PMMA as the standard (Entries 9−11), respectively. [d]MW ratios $M_{n,PI}/M_{n,X\ (X\ =\ PS/PMMA/P4VP)}$ were calculated according to the ^{1}H NMR spectra.

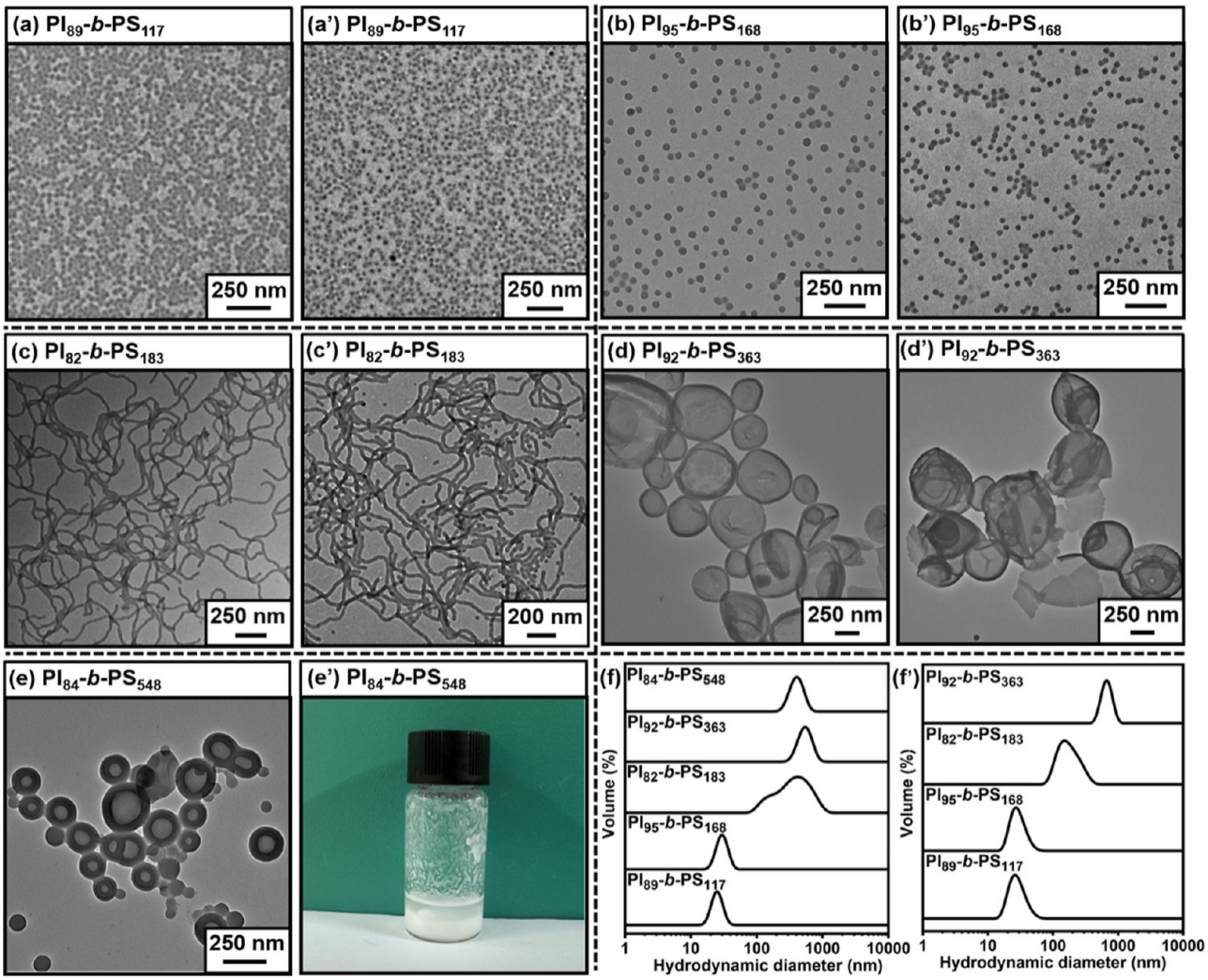

Figure 1. TEM images of PI-*b*-PS nano-objects (diluted into 0.01−0.3% w/w dispersions at 25 °C) prepared by the (a−e) LAP PISA process at 25 °C and (a'−e') HISA process at 90 °C with different MW ratios $M_{n,PI}/M_{n,PS}$ and fixed 20% w/w solids content. (f,f') DLS results of the corresponding nano-objects (diluted into 0.01−0.3% w/w dispersions at 25 °C).

https://doi.org/10.1021/acs.macromol.4c02808
Macromolecules 2025, 58, 4985−5000

exploring the HISA of additional BCPs (PI-*b*-PMMA/PI-*b*-P4VP) and the HICA of the AB_m/B_n (PI-*b*-$PMMA_m$/$PMMA_n$, PI-*b*-$P4VP_m$/$P4VP_n$) and AB_m/AC_n (PI-*b*-PS_m/PI-*b*-$PMMA_n$, PI-*b*-PS_m/PI-*b*-$P4VP_n$) systems. The corresponding dry T_g and solvated T_g (termed T_{sg}) of BCPs were characterized by differential scanning calorimetry (DSC) analysis. Finally, the possible morphological transformation mechanism of BCPs in the HISA process, as well as AB_m/B_n, AB_m/AB_n, and AB_m/AC_n systems in the HICA process, was elaborated.

RESULTS AND DISCUSSION

Preparation of the PI-*b*-PS-Based Nano-object via the HISA Process. In light of the previous work demonstrating that PI-*b*-PS-based nano-objects could be prepared by LAP PISA[25] and to explore the morphological differences between the nano-objects prepared by the HISA and LAP PISA processes, five PI-*b*-PS BCPs with different molecular weight (MW) ratios $M_{n,PI}/M_{n,PS}$ (**Entries 1−5** in Table 1) were selected as research models and first prepared using the LAP PISA process. Typically, *n*-heptane was used as the solvent at a fixed solids content of 20% w/w. The degree of polymerization (DP) of PI block (DP_{PI}) was kept within the range of 75−95, while the targeted DP of the chain-extended PS block (DP_{PS}) was systematically varied. These BCPs and their precursors were characterized by proton nuclear magnetic resonance (^{1}H NMR) and size exclusion chromatography (SEC) measurements, respectively. Based on the SEC results shown in Figure S1, DP_{PI} was calculated. This value was consistent with that obtained from the SEC equipped with a multiangle laser light scattering (MALLS) detector (Figure S2). Also, the relatively narrow molecular weight distribution (MWD) of the BCPs could be clearly discriminated from the SEC traces. As shown in the ^{1}H NMR spectrum in Figure S3, all of the characteristic proton signals of the PS and PI blocks could be clearly assigned. From these signals, $M_{n,PI}/M_{n,PS}$ and DP_{PS} values were calculated. The information for BCPs was also summarized and presented in Table 1.

As shown in Figure 1, in the LAP PISA process, the representative morphologies including spheres (Figure 1a,b), worms (Figure 1c), thin-walled vesicles (Figure 1d), and thick-walled vesicles (Figure 1e) were obtained from PI_{89}-*b*-PS_{117}, PI_{95}-*b*-PS_{168}, PI_{82}-*b*-PS_{183}, PI_{92}-*b*-PS_{363}, and PI_{84}-*b*-PS_{548} BCPs, respectively, as the length of the core-forming PS block increased. To compare the morphological differences between LAP PISA and HISA processes, the PI-*b*-PS BCPs generated in the LAP PISA process were first precipitated into methanol and dried in a vacuum oven at 45 °C. Subsequently, using *n*-heptane as the selective solvent, the dried PI-*b*-PS BCPs were treated at 90 °C for 1.0 h. Herein, the temperature setting of 90 °C was due to the limitation of the boiling point of *n*-heptane (98 °C). After the PI-*b*-PS BCPs were solvated or plasticized, the system was gradually cooled to room temperature (25 °C) at a stirring rate of 500 rpm. During the cooling process, the degree of solvation or plasticization of the core-forming PS block gradually decreased, and the BCP rearranged and self-assembled through a HISA process. As shown in Figure 1a',b', the TEM images for PI_{89}-*b*-PS_{117} and PI_{95}-*b*-PS_{168} revealed spherical nano-objects with a narrow size distribution similar to that observed in the LAP PISA process (Figure 1a,b). When the DP_{PS} was increased to 183, the worms formed by PI_{82}-*b*-PS_{183} in the LAP PISA process (Figure 1c) exhibited as a large area of wormlike morphologies with occasional spheres in the HISA process (Figure 1c'). For the DP_{PS} of 363, the vesicles prepared by PI_{92}-*b*-PS_{363} in the LAP PISA process (Figure 1d) turned into a mixture of vesicles and bits of lamellae in the HISA process (Figure 1d'). However, when the DP_{PS} was further increased to 548, it was unfortunately found that thick-walled vesicles obtained by PI_{84}-*b*-PS_{548} in the LAP PISA process (Figure 1e) became complete precipitates during the HISA process (Figure 1e'). Meanwhile, the DLS measurement provided consistent sizes with those from the TEM images (Figure 1f,f').

Similar to the LAP PISA process, the morphological evolution in the HISA process underwent a track from spheres to worms and eventually to vesicles with the increase of DP_{PS}. However, it should be noted that these two processes exhibited slight differences, especially in the case of PI_{84}-*b*-PS_{548}. This was because the nano-objects formed in LAP PISA and HISA processes might follow different self-assembly routes. The HISA process was implemented by directly placing the "frozen" BCP chains in a heated selective solvent. The degree of solvation or plasticization of the core-forming PS block and rearrangement ability of BCPs remained constant at a certain solvent and temperature in the HISA process. The morphologies formed in the HISA process reflected a thermodynamic equilibrium state. Differently, in the LAP PISA process, with the progress of chain extension, the degree of solvation or plasticization of the core-forming PS block and the rearrangement ability of BCP gradually decreased and became restricted. This resulted in regular morphological evolution of nano-objects, which reflected the kinetically trapped morphologies. To verify this deduction, four representative PI-*b*-PS nano-objects with different morphologies of spheres, worms, and vesicles prepared by the LAP PISA process were selected and subjected to a heating process at 90 °C for 2.0 h. As shown in Figure S4, the PI_{95}-*b*-PS_{168}, PI_{82}-*b*-PS_{183}, and PI_{92}-*b*-PS_{363} nano-objects retained their original morphologies of spheres (Figure S4a'), worms (Figure S4b'), and vesicles (Figure S4c'), respectively, indicating that the BCPs underwent effective rearrangement and self-assembly during both LAP PISA and HISA processes and a thermodynamic equilibrium state was reached. Differently, when PI_{84}-*b*-PS_{548} nano-objects prepared by the LAP PISA process were stored at room temperature (25 °C) for 20 days, the thick-walled vesicles could still be observed (Figure S5). However, once the PI_{84}-*b*-PS_{548} nano-objects were subjected to a heating process at 90 °C, their dispersion became heterogeneous and turned into a precipitate (Figure S 4d'), indicating that the thick-walled vesicles were kinetically trapped with a metastable morphology in the LAP PISA process. Meanwhile, the results confirmed that colloidal structures from the LAP PISA process were actually more plasticized than those formed in the HISA process. This was also the reason why the thick-walled vesicles could not be obtained through the HISA process of PI_{84}-*b*-PS_{548} BCP.

According to the literature mentioned in the Introduction,[49−51] there might be a UCST for the PI-*b*-PS BCPs in a certain solvent. However, in our study, additional experiments exhibited that the core-forming PS block had extremely low solubility in the employed *n*-heptane solvent at 90 °C. This confirmed the absence of a UCST below 90 °C. The reason might be due to the large differences in solubility parameters between *n*-heptane (15.3 $MPa^{1/2}$) and PS (18.6 $MPa^{1/2}$). Thus, it could be assumed that the PI-*b*-PS BCPs were merely plasticized, facilitating the rearrangement and self-assembly process. In this scenario, an order−order micellar transition

https://doi.org/10.1021/acs.macromol.4c02808
Macromolecules 2025, 58, 4985−5000

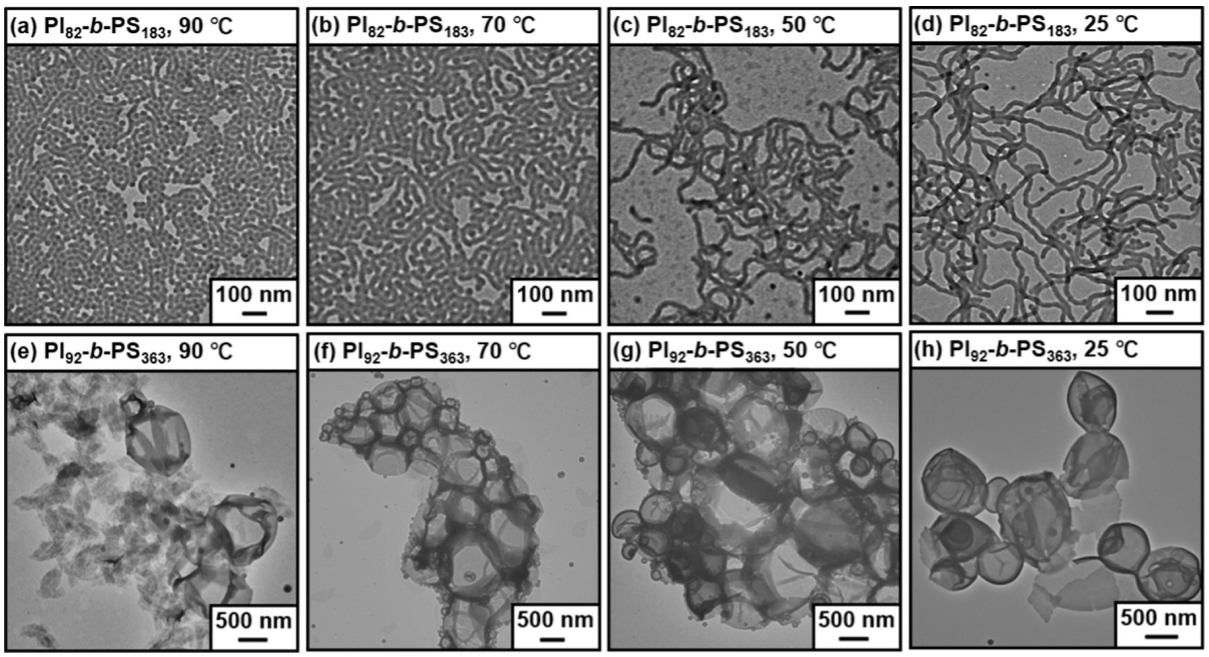

Figure 2. Morphological evolution of PI_{82}-*b*-PS_{183} and PI_{92}-*b*-PS_{363} nano-objects prepared by the HISA process at 90 °C in *n*-heptane with **a fixed solids** content of 20% w/w, diluted into 0.01−0.3% w/w dispersions and sampled TEM copper grids at (a,e) 90, (b,f) 70, (c,g) 50, and (d,h) 25 °C, respectively.

Scheme 2. Schematic Illustration of the HISA Process with Different PI-*b*-PS BCPs and Morphologies: (I,I') PI_{89}-*b*-PS_{117} and PI_{95}-*b*-PS_{168} (Spheres), (II,II') PI_{82}-*b*-PS_{183} (Worms), (III,III') PI_{92}-*b*-PS_{363} (Vesicles), and (VI,VI') PI_{84}-*b*-PS_{548} (Precipitate)[a]

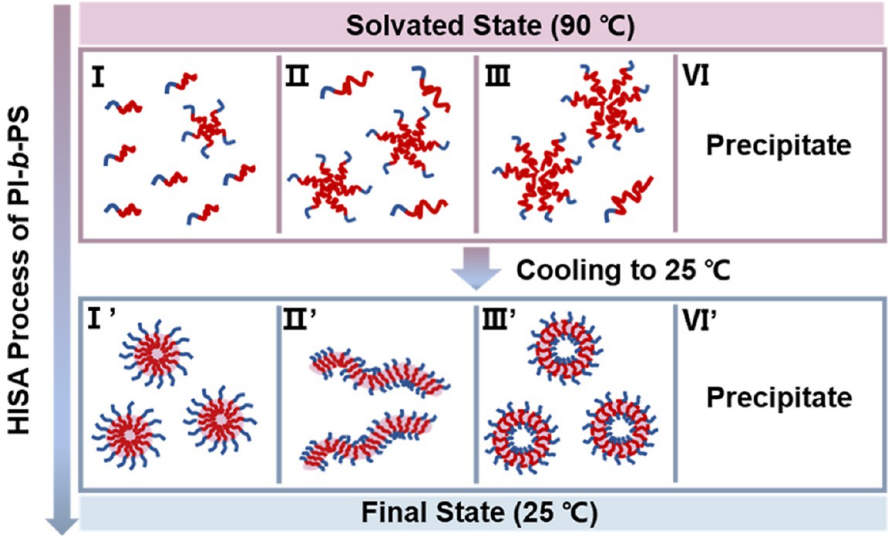

[a]Note: the red curves represent the core-forming PS block, and the blue curves represent the solvophilic PI block.

occurred, rather than the formation of a disordered state above the UCST. The deduction could be verified by monitoring the morphological evolution of PI-*b*-PS nano-objects during the cooling process from 90 to 70, 50, and 25 °C. Specifically, the PI_{82}-*b*-PS_{183} and PI_{92}-*b*-PS_{363} BCPs were first subjected to a heating process at 90 °C for 1.0 h and then a cooling process. At different cooling temperatures (90, 70, 50, and 25 °C), a quantified amount of self-assembly nano-objects was dispersed into preheated *n*-heptane at the corresponding temperatures with concentrations ranging from 0.01% to 0.3% w/w. The diluted dispersions maintained at the elevated temperatures were immediately dropped onto copper grids for subsequent TEM measurement. For PI_{82}-*b*-PS_{183} nano-objects, the spherical morphologies generated at 90 °C (Figure 2a) gradually transformed into short worms at 70 °C (Figure 2b), a mixture of long and short worms at 50 °C (Figure 2c), and ultimately long worms at 25 °C (Figure 2d). For PI_{92}-*b*-PS_{363} nano-objects, a mixture of fusiform lamellae and large vesicles was observed at 90 °C (Figure 2e). Subsequently, as the temperatures decreased, the morphologies gradually evolved into smaller regular vesicles with increased curvature (Figure 2f−h). Obviously, the morphologies were temperature-dependent due to the different degrees of solvation or plasticization of the core-forming PS block. Especially, the HISA process of PI_{82}-*b*-PS_{183} BCP was more sensitive to temperature, transforming from spheres to long worms. At

https://doi.org/10.1021/acs.macromol.4c02808
Macromolecules 2025, 58, 4985−5000

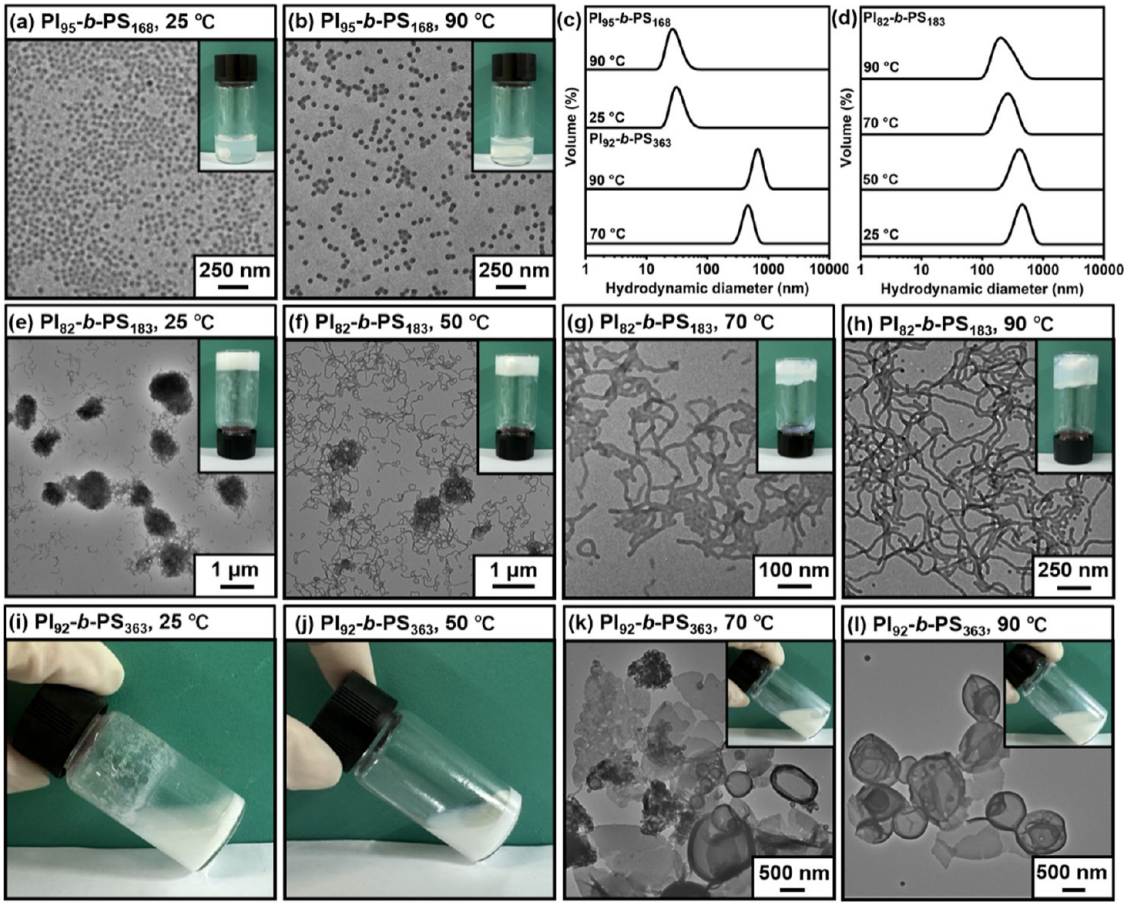

Figure 3. TEM images of (a,b) PI_{95}-*b*-PS_{168}, (e–h) PI_{82}-*b*-PS_{183}, and (i–l) PI_{92}-*b*-PS_{363} nano-objects (diluted into 0.01–0.3% w/w dispersions at 25 °C) prepared by the HISA process with **a fixed solids** content of 20% w/w and varying heating temperatures. (c,d) DLS results of the corresponding nano-objects (diluted into 0.01–0.3% w/w dispersions at 25 °C).

higher temperatures, the degree of solvation or plasticization of the core-forming PS block increased, improving the mobility of PS chains. Along with the shear force of agitation, the PI_{82}-*b*-PS_{183} BCP tended to form lower-order spheres or short worms, while the PI_{92}-*b*-PS_{363} BCP generated defective vesicles. When the temperature dropped to 25 °C, the plasticization and mobility of the core-forming PS block were greatly suppressed, driving further self-assembly of the BCPs. The HISA process is illustrated in Scheme 2. Actually, experiments on the morphological evolution of PI-*b*-PS nano-objects supported the formation of micellar nano-objects at 90 °C rather than a disordered state above the UCST, demonstrating the absence of UCST below 90 °C.

To further explore the mechanism of the HISA process, the influence of heating temperatures on the HISA process was investigated. Specifically, three representative PI-*b*-PS BCPs were selected to undergo the HISA process at varying heating temperatures of 25, 50, 70, and 90 °C for 1.0 h, respectively. When the PI_{95}-*b*-PS_{168} BCP was stirred at 25 °C for 1.0 h, a similar spherical morphology was obtained as that produced by the HISA process at 90 °C for 1.0 h (Figure 3a, b). DLS results showed nearly identical particle sizes (Figure 3c). For the PI_{82}-*b*-PS_{183} BCP, the macroscopic gels were formed through the HISA process at 25, 50, 70, and 90 °C for 1.0 h. By observation of the insets in Figure 3e–h, it could be discerned that the turbidity of gels gradually decreased as the heating temperatures increased. Higher turbidity indicated that the nano-objects in the dispersion had a higher degree of aggregation and larger particle sizes, leading to more light scattering. Further verification by TEM images showed that the nano-objects exhibited severely entangled short worms during the HISA process at 25 °C (Figure 3e). When the HISA process was conducted at 50 °C, the number of entangled worms decreased, while the number of dispersed worms increased (Figure 3f). As the heating temperatures rose to 70 and 90 °C, the length of the worms increased, and all the nano-objects were well dispersed (Figure 3g,h). When the DP_{PS} increased to 363, the PI_{92}-*b*-PS_{363} BCP had difficulty forming a stable dispersion, and macroscopic precipitation occurred at 25 °C (Figure 3i). Notably, the degree of precipitation decreased when the HISA process was implemented at 50 °C (Figure 3j). Further increasing the temperature to 70 and 90 °C resulted in the formation of milky dispersions along with the generation of vesicles. Moreover, the vesicles formed at 90 °C were more intact than those at 70 °C (Figure 3k,l). These results demonstrated that the degree of solvation or plasticization of the core-forming PS block depended greatly on both heating temperatures and the DP_{PS}. Generally, within the temperature range of 25–90 °C, the use of relatively higher temperatures and lower DP_{PS} values can enhance the degree of the solvation or plasticization of BCPs, thus favoring the formation of regular morphologies.

In summary, when keeping the solvent (*n*-heptane) and **solids** content (20% w/w) the same for both the HISA and LAP PISA processes, despite the different self-assembly routes, only slight morphological differences could be observed.

https://doi.org/10.1021/acs.macromol.4c02808
Macromolecules 2025, 58, 4985–5000

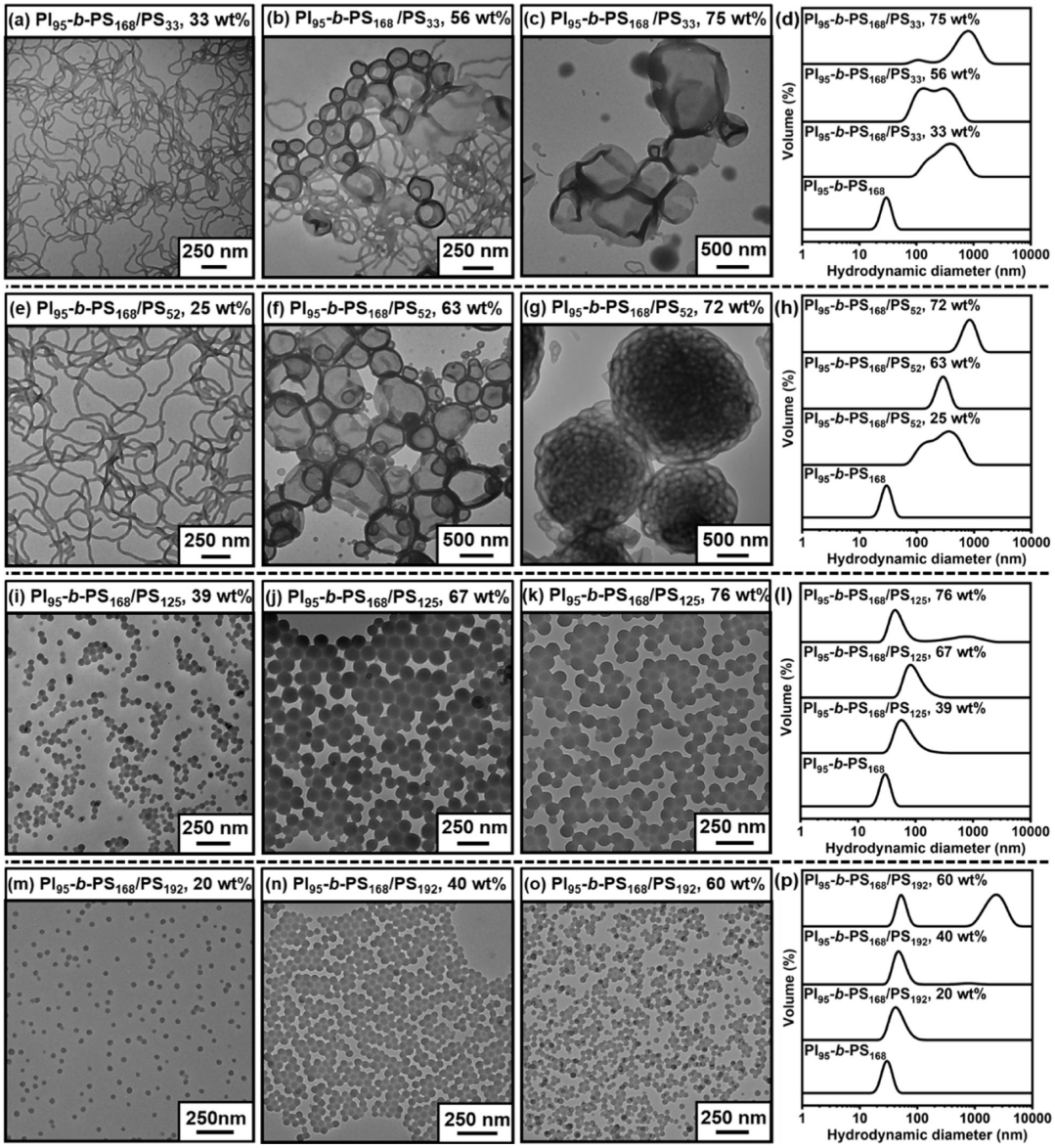

Figure 4. TEM images of PI_{95}-*b*-PS_{168}/PS_n nano-objects (diluted into 0.01−0.3% w/w dispersions at 25 °C) formed in the HICA process at 90 °C with **fixed 20% w/w solids** content and varying DP_{PS} of the PS homopolymer: (a−c) PS_{33}, (e−g) PS_{52}, (i−k) PS_{125}, and (m−o) PS_{192}. (d,h,l,p) DLS results of the corresponding nano-objects (diluted into 0.01−0.3% w/w dispersions at 25 °C). Note: The percentage represents the PS homopolymer content as a proportion of all PS chains.

Notably, the HISA process reflected a thermodynamic equilibrium state, which was dominantly modulated by the degree of solvation or plasticization of the core-forming PS block. Relatively higher heating temperatures and lower DP_{PS} values promoted a higher degree of solvation and plasticization. Additionally, the HISA process started directly from the purified solid BCPs, thereby avoiding contaminants from monomers, catalysts, or initiators. Additionally, the HISA process differed from the commonly used solvent-switching technique,[58−60] in which a good solvent for both blocks was first added and then removed through evaporation or dialysis. Therefore, the simplicity of the HISA process greatly facilitated the preparation of nano-objects.

Preparation of PI-*b*-PS_m/PS_n (AB_m/B_n) Blend-Based Nano-objects via the HICA Process. Out of interest in obtaining higher-order morphologies and as an extension of the HISA technique, the HICA process of PI-*b*-PS_m/PS_n blends was investigated. Compared with the intricate procedure of polymerization-induced cooperative assembly (PICA),[26,28,31,56,57] where nano-objects were obtained by combining a presynthesized macromolecular initiator with a small-molecular initiator to simultaneously initiate polymerization and form a BCP and solvophobic homopolymer, the HICA process facilitated cooperative self-assembly through a simple operation. Specifically, it involved mixing BCPs and homopolymers in selective solvents, followed by a thermal cycle. The PI_{95}-*b*-PS_{168}/PS_n-based HICA process with varying DP_{PS} and content of the PS homopolymer was explored (Table S1). Using the LAP process, PS homopolymers with different DPs (PS_{33}, PS_{52}, PS_{125}, PS_{192}) and narrow M_w/M_n were successfully synthesized (Figure S6). Similar to the aforementioned HISA process, we used *n*-heptane as a selective solvent with **a solids content** of 20% w/w. Nano-objects were prepared by heating PI_{95}-*b*-PS_{168}/PS_n blends at 90 °C for 1.0 h

https://doi.org/10.1021/acs.macromol.4c02808
Macromolecules 2025, 58, 4985−5000

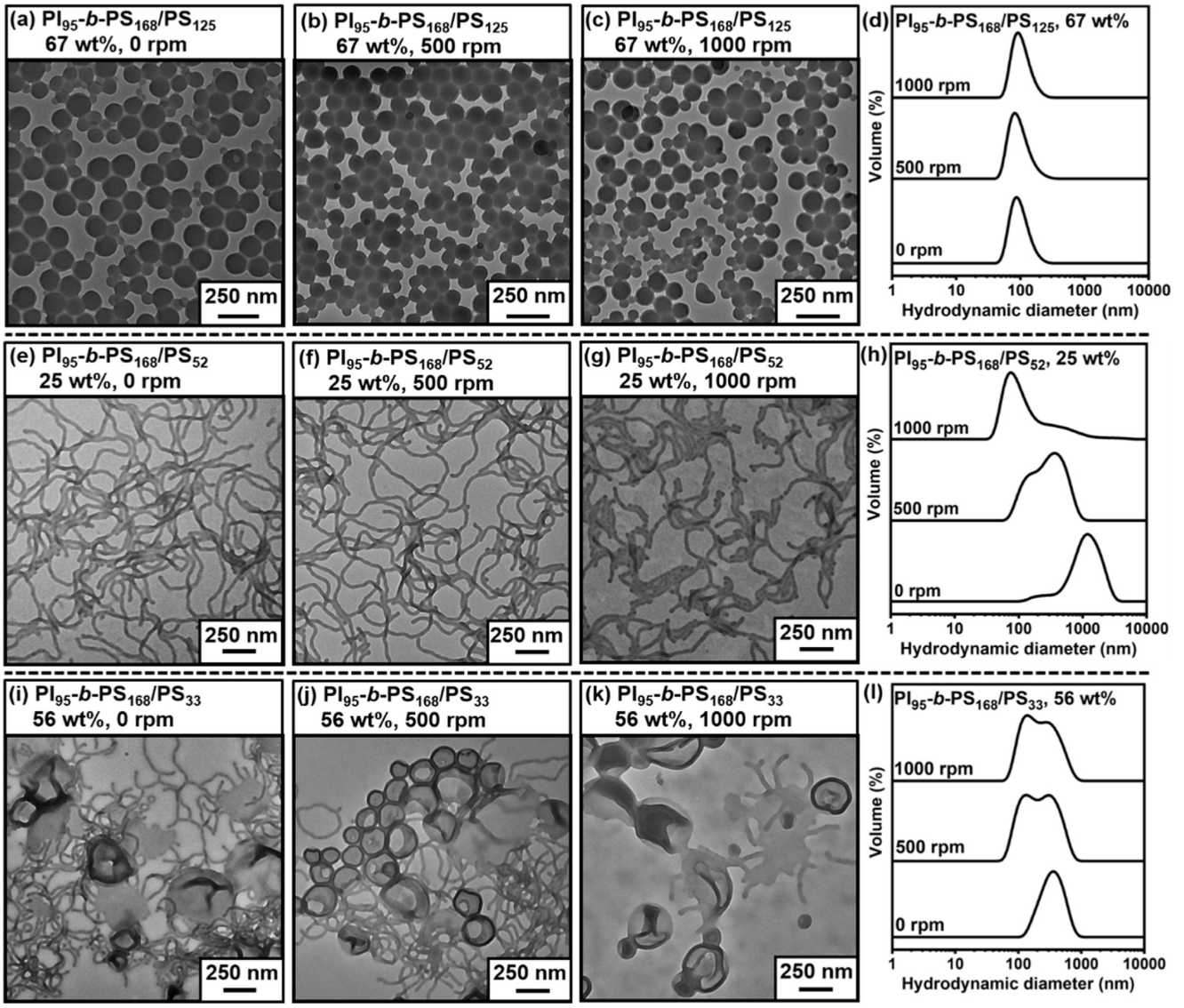

Figure 5. TEM images of PI_{95}-*b*-PS_{168}/PS_n nano-objects (diluted into 0.01−0.3% w/w dispersions at 25 °C) formed in the HICA process at 90 °C using 20% w/w solids content with varying DP_{PS} of the PS homopolymer: (a−c) PS_{125}, (e−g) PS_{52}, (i−k) PS_{33}, and different stirring rates during the cooling stage: (a, e, (i) 0 rpm, (b,f,j) 500 rpm, and (c,g,k) 1000 rpm. (d,h,l) DLS results of the corresponding nano-objects (diluted into 0.01−0.3% w/w dispersions at 25 °C). Note: The percentage represents the PS homopolymer content as a proportion of all PS chains.

and then cooling to 25 °C under a stirring rate of 500 rpm (Figure 4).

First, when the homopolymer PS_{33} was introduced into the HICA system, significant morphological changes were observed compared to the PI_{95}-*b*-PS_{168} nano-objects (spheres with an average diameter of 21 ± 11 nm, Figure 1b'). As the content of PS_{33} increased from 33 wt % to 56 and 75 wt %, the morphologies underwent a sequential transformation from worms (Figure 4a) to a mixture of worms and vesicles (Figure 4b) and finally to vesicles (Figure 4c). The DLS curves (Figure 4d) showed consistent results with those from the TEM images. Subsequently, when the DP_{PS} of the PS homopolymer was increased and PS_{52} was added, higher-order morphologies such as worms (Figure 4e), vesicles (Figure 4f), and sponges (Figure 4g) emerged with an increasing content of PS_{52}. These results were consistent with those of the PICA process in our previous work.[26] However, when the DP_{PS} was further increased and PS_{125} or PS_{192} was involved, only spheres were collected in all cases, and no significant morphological changes were observed (Figure 4i−o).

Additionally, in the HICA process, the effect of stirring rates (0, 500, 1000 rpm) during the cooling stage on morphological formation of nano-objects was also investigated (Figure 5). For the spherical PI_{95}-*b*-PS_{168}/PS_{125} nano-objects, as revealed by the TEM images (Figure 5a−c) and the relevant DLS results (Figure 5d), the stirring rate had a negligible influence on the morphological evolution, and the particle sizes of these nano-objects remained nearly unchanged. Conversely, the stirring rate had a great influence on the morphological evolution of the worm-like PI_{95}-*b*-PS_{168}/PS_{52} nano-objects. Specifically, as the stirring rate increased from 0 to 1000 rpm, the length of the worms gradually decreased (Figure 5e−g), which was also verified by the corresponding DLS results shown in Figure 5h. This could be attributed to the fact that worms were more sensitive to the shear forces generated by the stirring rates compared to spheres. For the PI_{95}-*b*-PS_{168}/PS_{33} nano-objects, vesicles were obtained at a stirring rate of 500 rpm. When the

https://doi.org/10.1021/acs.macromol.4c02808
Macromolecules 2025, 58, 4985−5000

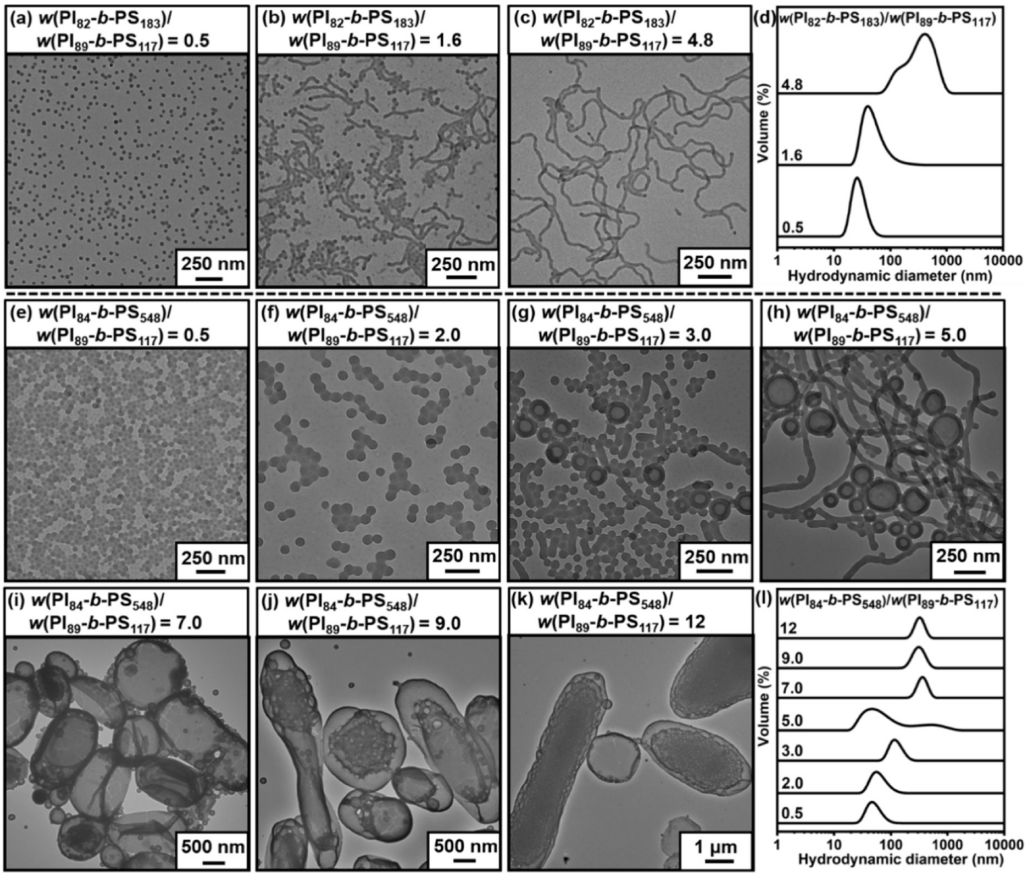

Figure 6. TEM images of binary blend-based nano-objects (diluted into 0.01−0.3% w/w dispersions at 25 °C) formed in the HICA process using a solids content of 20% w/w and varying weight ratio $w(PI_{82}\text{-}b\text{-}PS_{183})/w(PI_{89}\text{-}b\text{-}PS_{117})$ of (a) 0.5, (b) 1.6, and (c) 4.8 and $w(PI_{84}\text{-}b\text{-}PS_{548})/w(PI_{89}\text{-}b\text{-}PS_{117})$ of (e) 0.5, (f) 2.0, (g) 3.0, (h) 5.0, (i) 7.0, (j) 9.0, and (k) 12. (d,l) DLS results of the corresponding nano-objects (diluted into 0.01−0.3% w/w dispersions at 25 °C).

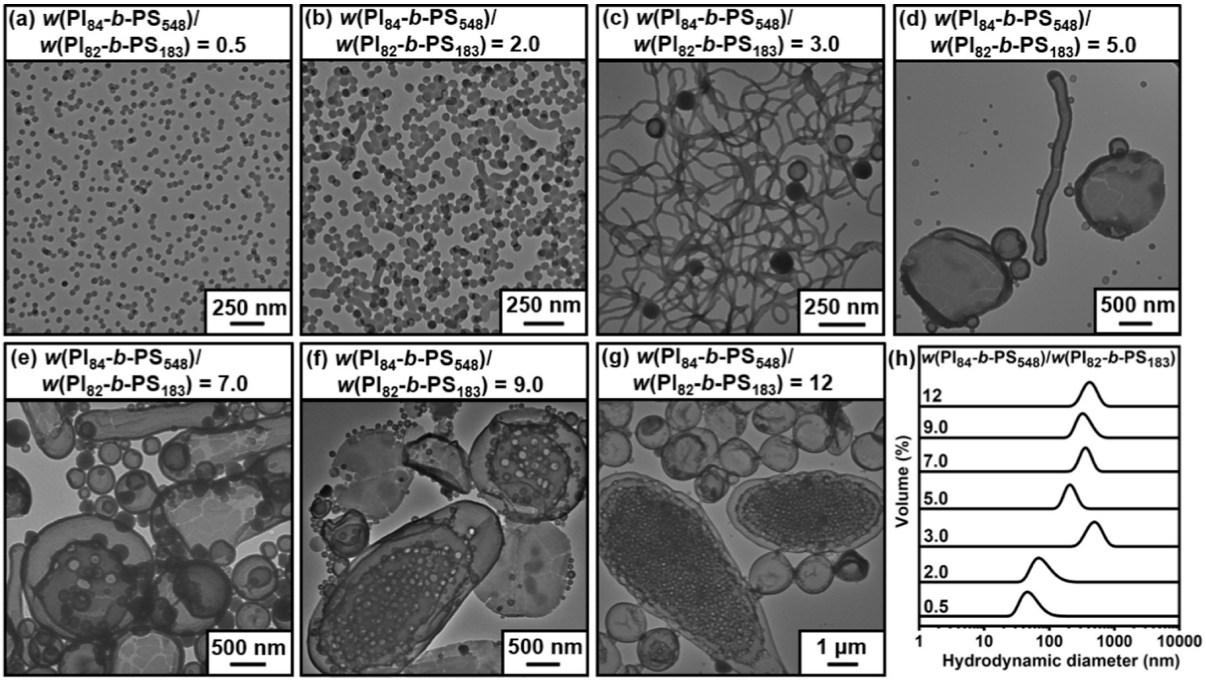

Figure 7. TEM images of binary blend-based nano-objects (diluted into 0.01−0.3% w/w dispersions at 25 °C) formed in the HICA process at 90 °C using a solids content of 20% w/w and varying weight ratio $w(PI_{84}\text{-}b\text{-}PS_{548})/w(PI_{82}\text{-}b\text{-}PS_{183})$ of (a) 0.5, (b) 2.0, (c) 3.0, (d) 5.0, (e) 7.0, (f) 9.0, and (g) 12. (h) DLS results of the corresponding nano-objects (diluted into 0.01−0.3% w/w dispersions at 25 °C).

https://doi.org/10.1021/acs.macromol.4c02808
Macromolecules 2025, 58, 4985−5000

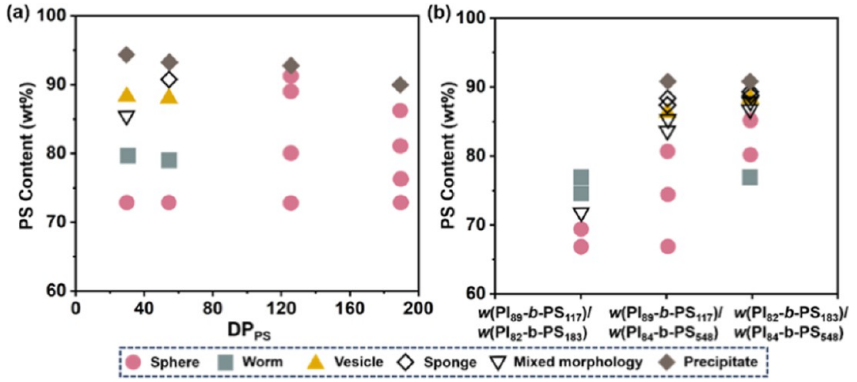

Figure 8. Pseudophase diagrams of (a) PI_{95}-*b*-PS_{168}/PS_n nano-objects based on the variation of PS content (as a proportion of all polymer chains) and DP_{PS} **at a solids content** of 20% w/w and (b) a binary copolymer blended system based on different PS contents (as a proportion of all polymer chains) **at a solids content** of 20% w/w.

Scheme 3. Schematic Illustration of the HICA Process of PI_{95}-*b*-PS_{168}/PS_n with Different Morphologies[a]

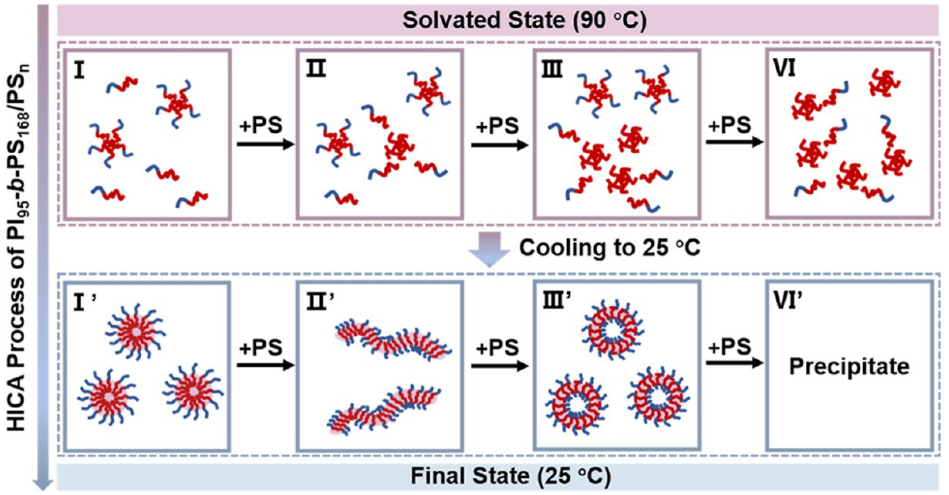

[a]Note: the red curves represent the core-forming PS block, and the blue curves represent the solvophilic PI block.

stirring rate was decreased to 0 rpm, only a mixture of worms, lamellae, and a few thin-walled vesicles could be captured (Figure 5i). Alternatively, high-speed stirring at 1000 rpm resulted in the formation of a mixture of octopus-like structures and broken vesicles (Figure 5k). The relatively lower-order morphologies in the former case (0 rpm) were probably due to the low efficiency of collision and fusion among the nano-objects. In contrast, the stronger shear forces in the latter case (1000 rpm) accelerated the transformation of worms into octopus-like structures, while some vesicles were destroyed due to the high stirring rate.

Preparation of PI-*b*-PS_m/PI-*b*-PS_n (AB_m/AB_n) Blend-Based Nano-objects via the HICA Process. Aiming to further explore the advantages of the HICA process, we adjusted the morphologies of the self-assembled nano-objects by simple mixing of PI-*b*-PS BCPs rather than a demanding synthetic approach in the LAP PISA or LAP PICA processes. Specifically, three samples including PI_{89}-*b*-PS_{117} (shown as spheres in the HISA process, Figure 1a'), PI_{82}-*b*-PS_{183} (shown as worms in the HISA process, Figure 1c'), and PI_{84}-*b*-PS_{548} (shown as precipitates in the HISA process, Figure 1e') were pairwise mixed in *n*-heptane at varying weight ratios (Table S2). The mixtures then underwent a heating (90 °C for 1.0 h) and cooling (25 °C) cycle with a stirring rate of 500 rpm. The morphologies and sizes of the obtained nano-objects in the HICA process were characterized by TEM and DLS, respectively.

Figure 6 showed the results of the cooperative self-assembly of PI_{89}-*b*-PS_{117} and PI_{82}-*b*-PS_{183} BCPs via the HICA process. As the weight ratio $w(PI_{82}\text{-}b\text{-}PS_{183})/w(PI_{89}\text{-}b\text{-}PS_{117})$ increased from 0.5 to 1.6 and then to 4.8, the morphologies underwent predictable changes from spheres (Figure 6a) to a mixture of spheres and short worms (Figure 6b) and finally to long worms (Figure 6c). To broaden the scope of blending, PI_{84}-*b*-PS_{548} BCP with a larger DP_{PS} was selected to blend with PI_{89}-*b*-PS_{117} BCP. As the weight ratio $w(PI_{84}\text{-}b\text{-}PS_{548})/w(PI_{89}\text{-}b\text{-}PS_{117})$ increased from 0.5 to 2.0, 3.0, 5.0, 7.0, 9.0, and 12, corresponding morphological transformations from spheres (Figure 6e, f) to a mixture of spheres, worms, and vesicles (Figure 6g), a mixture of worms and vesicles (Figure 6h), large ellipsoidal vesicles (Figure 6i), and finally to sponges (Figure 6j,k) were observed.

Similarly, the morphological evolution of binary blended PI_{82}-*b*-PS_{183} and PI_{84}-*b*-PS_{548} in the HICA process was investigated by modulating the weight ratio $w(PI_{84}\text{-}b\text{-}PS_{548})/w(PI_{82}\text{-}b\text{-}PS_{183})$. Surprisingly, when $w(PI_{84}\text{-}b\text{-}PS_{548})/w(PI_{82}\text{-}b\text{-}PS_{183})$ was designed as 0.5 and 2.0, lower-order morphologies of spheres rather than both worms and vesicles were captured

https://doi.org/10.1021/acs.macromol.4c02808
Macromolecules 2025, 58, 4985−5000

(Figure 7a,b). When $w(PI_{84}\text{-}b\text{-}PS_{548})/w(PI_{82}\text{-}b\text{-}PS_{183})$ was further increased, the TEM images showed a sequence of morphological evolution from a mixture of worms and vesicles ($w(PI_{84}\text{-}b\text{-}PS_{548})/w(PI_{82}\text{-}b\text{-}PS_{183})$ = 3.0, Figure 7c) to a mixture of large vesicles and nanotubes ($w(PI_{84}\text{-}b\text{-}PS_{548})/w(PI_{82}\text{-}b\text{-}PS_{183})$ = 5.0, Figure 7d), a mixture of large vesicles, nanotubes, and compound vesicles ($w(PI_{84}\text{-}b\text{-}PS_{548})/w(PI_{82}\text{-}b\text{-}PS_{183})$ = 7.0, Figure 7e), and a mixture of vesicles and sponges ($w(PI_{84}\text{-}b\text{-}PS_{548})/w(PI_{82}\text{-}b\text{-}PS_{183})$ = 9.0 and 12, Figure 7f,g), respectively.

Explanation on the Morphological Evolution of Nano-objects in the HICA Process. To summarize the morphological evolution of PI-*b*-PS_m/PS_n (AB_m/B_n) and PI-*b*-PS_m/PI-*b*-PS_n (AB_m/AB_n) nano-objects in the HICA process, the pseudophase diagrams were constructed. To distinguish the difference of the HICA process in these two cases, we calculated the PS content as a proportion of all polymer chains in the HICA formulation and set it as the vertical ordinate. The DP_{PS} of homopolymer (Figure 8a) or binary blends was labeled as the horizontal ordinate (Figure 8b).

As shown in Figure 8a, when PS_{33} or PS_{52} homopolymers were involved in PI_{89}-*b*-PS_{168} BCPs, a higher PS content as a proportion of all polymer chains promoted morphological transitions. This phenomenon could be explained by the packing parameter $P = v/a_0l_c$ (where v, a_0, and l_c represent the volume of the core-forming block, the interfacial area, and the length of the core-forming block, respectively). The packing parameter was determined by a force balance among the stretching of the core-forming blocks, the interfacial tension between the core and the solvent, and intercorona interactions.[61−63] Under these circumstances, the high operation temperature (90 °C), which was above the solvated T_{sg} (16 °C, Figure S12b) of the core-forming PS block, led to the solvation or plasticization of the solvophobic PS block or homopolymer. As the temperature gradually decreased, the solvated or plasticized solvophobic PS homopolymer tended to aggregate near the core because of its lack of self-stabilizing ability. This subsequently induced the adsorption of the "BCP surfactant" to stabilize itself in the solvent (Scheme 3).[26,28,64] This process implied an increase of the core-forming volume (v) and, meanwhile, a significant reduction in the stretching extent of the solvophobic block (l_c). As a result, the P value increased and manifested as a transformation from spheres to higher-order morphologies. However, introducing PS_{125} and PS_{192} with higher DP_{PS} into PI_{89}-*b*-PS_{168} exclusively resulted in spherical morphologies. This could be due to the decreased solvation or plasticization of the micellar core caused by the excessively long PS homopolymers. Consequently, spheres with a minimum interfacial energy were preferred. Additionally, compared with the LAP PICA process,[26] smaller-sized spheres were captured in the HICA process when the content of PS_{125} (Figure 4j,k) and PS_{192} (Figure 4n,o) was further increased. This was probably because the system had reached the maximum degree of solvation or plasticization at 90 °C. At this moment, even if the content of the homopolymer increased, the plasticization volume (v) of the core-forming block would not increase. Instead, a small amount of the precipitate appeared (as illustrated by the DLS curves in Figure 4l,p), and the corresponding TEM (Figure 4k,o) exhibited spheres in the unprecipitated section. In general, in the PI_{95}-*b*-PS_{168}/PS_n system (Figure 8a), a lower DP_{PS} of the PS homopolymer (33 or 52) promoted the formation of higher-order morphologies as the content of PS in the total polymers increased. However, a higher DP_{PS} of the PS homopolymer resulted in only spheres.

Alternatively, when BCPs with similar DP_{PI} but different DP_{PS} (PI_{82}-*b*-PS_{183} and PI_{84}-*b*-PS_{548}) were mixed with PI_{89}-*b*-PS_{117}, worms (HICA process of PI_{89}-*b*-PS_{117}/PI_{82}-*b*-PS_{183}, Figure 6c), vesicles, sponges, and mixed morphologies (HICA process of PI_{89}-*b*-PS_{117}/PI_{84}-*b*-PS_{548}, Figure 6g−k) were caught with the increase of the total PS content. In these cases, unlike the single spheres formed in the HICA process of the PI_{95}-*b*-PS_{168}/PS_{125} and PI_{95}-*b*-PS_{168}/PS_{192} systems, a higher PS content as a proportion of all polymer chains led to the formation of higher-order morphologies (Figure 8b). This could be attributed to the enhanced stabilization effect of PI chains in binary BCP blends compared to blends mixed only with the PS homopolymer, while the total PS content remained similar, thus facilitating the further transformation into thermodynamically stable higher-order morphologies, such as worms and vesicles. In addition, investigation of PI_{89}-*b*-PS_{117}/PI_{84}-*b*-PS_{548} and PI_{82}-*b*-PS_{183}/PI_{84}-*b*-PS_{548} systems revealed that, under similar total PS content, the former exhibited more rapid morphological transformation. This disparity stemmed from the larger DP difference of the solvophobic PS block in the former system (ΔDP_{PS} = 431) compared to that in the latter (ΔDP_{PS} = 366). According to the thermodynamic stability mechanism, the greater asymmetry of core-forming chains in the former system endowed it with higher conformational entropy, thus driving faster morphological transitions.

Another noteworthy phenomenon in the PI_{82}-*b*-PS_{183}/PI_{84}-*b*-PS_{548} system was that only spheres were captured when the total PS content in the HICA formulation was modulated as 82 and 86 wt %. This seemed abnormal because PI_{82}-*b*-PS_{183} and PI_{84}-*b*-PS_{548} formed worms (Figure 1c') and precipitates (Figure 1e'), respectively, in the HISA system. When PI_{82}-*b*-PS_{183} and PI_{84}-*b*-PS_{548} were mixed in *n*-heptane at 90 °C, the BCPs were plasticized and underwent kinetic rearrangement to form primary micelles. However, due to the extremely long solvophobic PS block in PI_{84}-*b*-PS_{548}, the primary micelles quickly reached the solvation limit as the temperature decreased. They tended to precipitate, triggering the adsorption of short-chain BCP "surfactants" (PI_{82}-*b*-PS_{183}) for stabilization. To minimize the entropy penalty associated with chain stretching, spontaneous arrangement and fusion of the chains between the two BCPs occurred, resulting in the formation of thermodynamically stable spheres. Hence, the HICA process between two BCPs was not simply an "addition" of the morphologies. The BCPs decoupled from the self-assembly process were like "eliminating the thermal history", and they would continuously arrange during the heating-solvation and cooling-self-assembly processes to reach the most thermodynamically stable state.

In short, multiple morphologies were successfully achieved by regulating the mixing ratios of BCPs with BCPs or PS homopolymers in the HICA process. The rearrangement and interaction of core-forming chains with different lengths and compositions enabled the successful formation of larger spherical vesicles, ellipsoidal vesicles, nanotubes, and sponges. This bridged the gap between simple self-assembly and sophisticated morphologies through the cooperative effect in the HICA process.

Development of HISA and HICA Processes beyond PI-*b*-PS BCP. To evaluate the universality of the HISA and HICA techniques, PI-*b*-PMMA and PI-*b*-P4VP, as well as

https://doi.org/10.1021/acs.macromol.4c02808
Macromolecules 2025, 58, 4985−5000

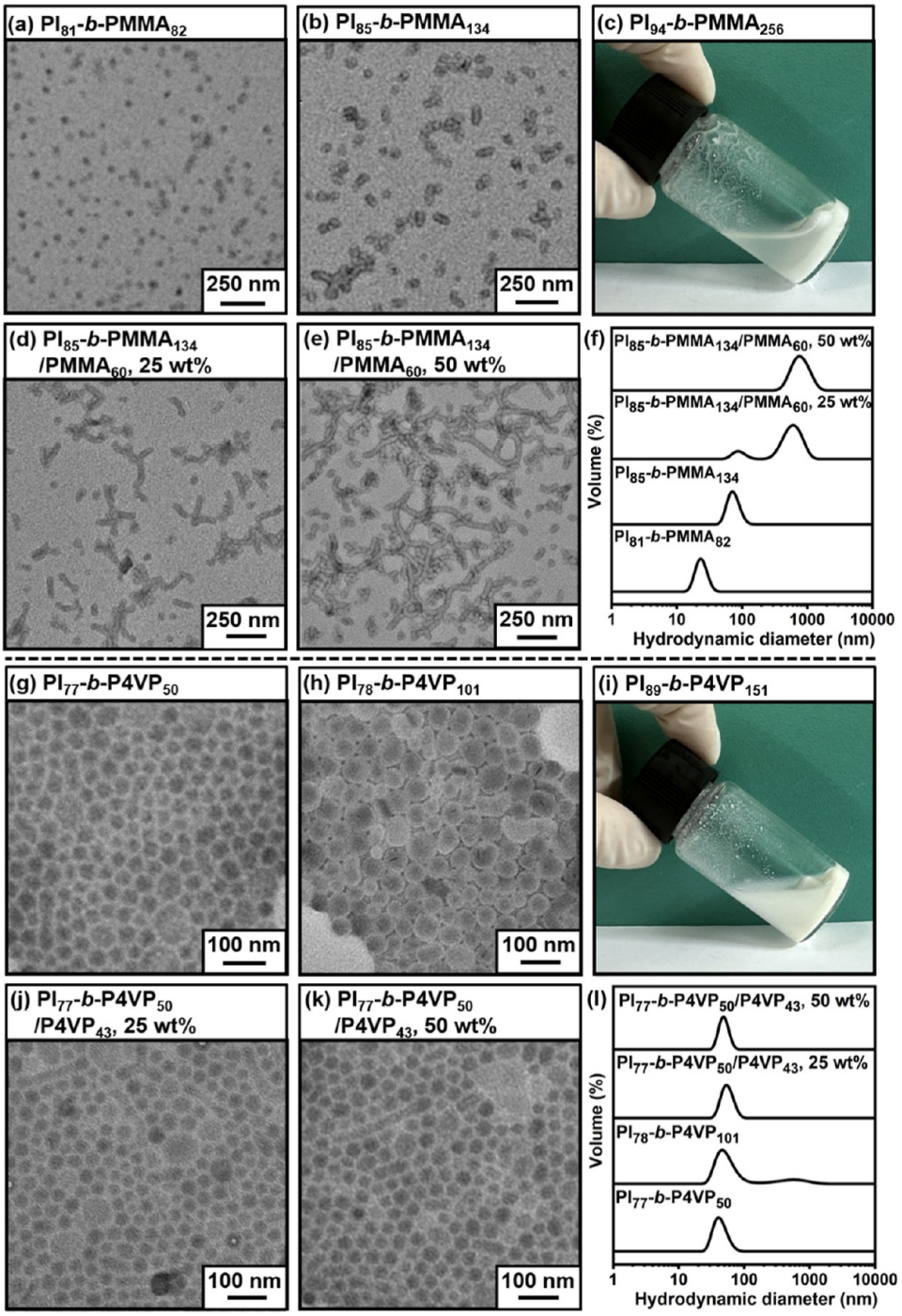

Figure 9. TEM images of (a−c) PI-*b*-PMMA nano-objects prepared by the HISA process at 90 °C with different MW ratio $M_{n,PI}/M_{n,PMMA}$, (d,e) PI-*b*-PMMA$_m$/PMMA$_n$ nano-objects prepared by the HICA process at 90 °C with varying PMMA$_{60}$ homopolymer content as a proportion of all PMMA chains, (g−i) PI-*b*-P4VP nano-objects prepared by the HISA process at 90 °C with different MW ratio $M_{n,PI}/M_{n,P4VP}$, and (j,k) PI-*b*-P4VP$_m$/P4VP$_n$ nano-objects prepared by the HICA process at 90 °C with varying P4VP$_{43}$ homopolymer content as a proportion of all P4VP chains using 20% w/w solids content (diluted into 0.01−0.3% w/w dispersions at 25 °C). (f,l) DLS results of the corresponding nano-objects (diluted into 0.01−0.3% w/w dispersions at 25 °C).

blends of PI-*b*-PMMA$_m$/PMMA$_n$ and PI-*b*-P4VP$_m$/P4VP$_n$, were involved. The PI-*b*-PMMA (**Entries 6−8** in Table 1) and PI-*b*-P4VP (**Entries 9−11** in Table 1) BCPs with different $M_{n,PI}/M_{n,X\ (X=PMMA/P4VP)}$, as well as PMMA$_{60}$ and P4VP$_{43}$ homopolymers were successfully synthesized by LAP and characterized by ^{1}H NMR (Figure S7) and SEC measurements (Figure S8 and S9), respectively. Similarly, the HISA and HICA processes were conducted by heating at 90 °C for 1.0 h in *n*-heptane and then cooling to 25 °C at a stirring rate of 500 rpm with a solids content of 20% w/w. The detailed formulations and the corresponding morphologies were summarized in Table S3.

The generated nano-objects were characterized using TEM and DLS measurements. As depicted in Figure 9, the morphological window of PI-*b*-PMMA nano-objects was notably narrower compared to that of PI-*b*-PS BCPs in the

https://doi.org/10.1021/acs.macromol.4c02808
Macromolecules 2025, 58, 4985−5000

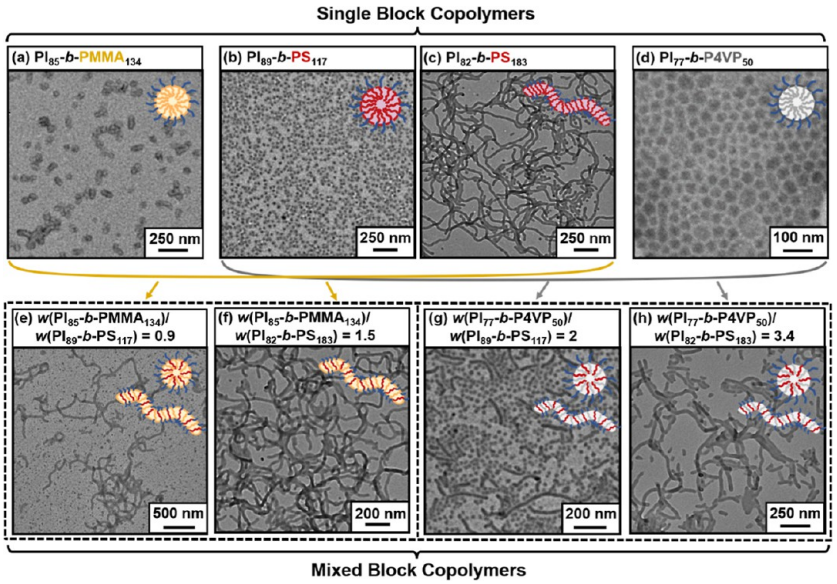

Figure 10. TEM images of (a−d) HISA of single BCPs and (e−h) HICA process of mixed BCPs (diluted into 0.01−0.3% w/w dispersions at 25 °C) at 90 °C in *n*-heptane with 20% w/w solids content.

HISA process (Figure 1). As the DP_{PMMA} of the core-forming PMMA block increased, only spherical morphologies were observed (Figure 9a,b). Additionally, macroscopic precipitation occurred when DP_{PMMA} approached approximately 256 for PI_{94}-*b*-$PMMA_{256}$ BCP. Alternatively, when incorporating the $PMMA_{60}$ homopolymer into the PI-*b*-PMMA/$PMMA_{60}$ system, a morphological transition from spheres (Figure 9b) to a mixture of spheres and short worms (Figure 9d) and finally to long worms (Figure 9e) was observed. However, for PI-*b*-P4VP (Figure 9g−i) and PI-*b*-P4VP/$P4VP_{43}$ nano-objects (Figure 9j,k), we found that regardless of varying the DP_{P4VP} of the BCPs in the HISA system or the $P4VP_{43}$ homopolymer content as a proportion of all P4VP chains in the HICA system, there were minimal morphological changes. The nano-objects always remained as spheres.

To further expand the application of the HICA process in constructing multicomponent nano-objects, BCPs with distinct chemical compositions (AB_m/AC_n) were blended and incorporated into the HICA system. Specifically, PI_{89}-*b*-PS_{117} (shown as spheres in the HISA process, Figure 10b) and PI_{82}-*b*-PS_{183} (shown as worms in the HISA process, Figure 10c) were blended with PI_{85}-*b*-$PMMA_{134}$ (shown as spheres in the HISA process, Figure 10a) and PI_{77}-*b*-$P4VP_{50}$ (shown as spheres in the HISA process, Figure 10d), respectively. The weight ratio of the two BCPs was designed to ensure an equal weight percentage of the core-forming B and C blocks. The corresponding morphological results were presented in Figure 10e−h. On the one hand, when we carried out the HICA process of PI_{85}-*b*-$PMMA_{134}$/PI_{89}-*b*-PS_{117} or PI_{77}-*b*-$P4VP_{50}$/PI_{89}-*b*-PS_{117} in *n*-heptane, a mixture of spheres and worms was formed (Figure 10e, g). This morphology was clearly different from the spherical morphology of the individual BCPs of PI_{85}-*b*-$PMMA_{134}$, PI_{77}-*b*-$P4VP_{50}$, or PI_{89}-*b*-PS_{117}. On the other hand, the HICA process of PI_{85}-*b*-$PMMA_{134}$ (shown as spheres in the HISA process, Figure 10a) and PI_{82}-*b*-PS_{183} (shown as worms in the HISA process, Figure 10c) showed that the spherical morphology completely disappeared and transformed into worms (Figure 10f). In the case of the HICA process between PI_{77}-*b*-$P4VP_{50}$ (shown as spheres in the HISA process, Figure 10d) and PI_{82}-*b*-PS_{183} (shown as worms in the HISA process, Figure 10c), a mixture of spheres and worms was generated (Figure 10h), as evidenced by the corresponding DLS results shown in Figure S10.

To verify whether the AB_m/AC_n nano-objects obtained from the HICA process were a mixture of homogeneous nano-objects or nano-objects consisting of block copolymer blends, the weight ratio w(PI_{77}-*b*-$P4VP_{50}$)/w(PI_{82}-*b*-PS_{183}) was fixed as 3.4 and two additional comparative experiments were designed. Specifically, we blended the powders of PI_{77}-*b*-$P4VP_{50}$ and PI_{82}-*b*-PS_{183} BCPs at 25 °C and also blended the PI_{77}-*b*-$P4VP_{50}$ and PI_{82}-*b*-PS_{183} nano-objects prepared by the HISA process at 25 °C. As shown in Figure S11, when the powder of the two BCPs was blended at 25 °C, the macroscopic precipitation occurred (Figure S11a). When the PI_{77}-*b*-$P4VP_{50}$ (shown as spheres in the HISA process, Figure 9g) and PI_{82}-*b*-PS_{183} (shown as worms in the HISA process, Figure 1c') nano-objects were blended at 25 °C, a mixture of spheres and worms was observed, with no sign of morphological fusion (Figure S11c). In contrast, during the HICA process starting from the same proportion of PI_{77}-*b*-$P4VP_{50}$ and PI_{82}-*b*-PS_{183} BCP powders, no precipitation was observed in the system after heating at 90 °C. Moreover, more worms were discernible, and spheres almost disappeared (Figure S11b). These results indicated that in the HICA process, the PI_{82}-*b*-PS_{183}/PI_{77}-*b*-$P4VP_{50}$ (AB_m/AC_n) BCPs formed a core with mixed PS and P4VP blocks. Correspondingly, the interactions and fusions between PS and P4VP blocks led to morphologies distinct from those of the original individual spheres and worms.

As shown above, the universality of the HISA and HICA techniques has been comprehensively confirmed. To gain further insights into the mechanism of the HISA and HICA processes, DSC analysis on three representative BCPs (PI_{95}-*b*-PS_{168}, PI_{85}-*b*-$PMMA_{134}$, and PI_{77}-*b*-$P4VP_{50}$) in both the dry state and the solvated state in *n*-heptane was conducted. The results were presented in Figure S12. The potential mechanism underlying the phenomena can be elucidated as follows. First, compared to the PI-*b*-PS BCP, the HISA processes of PI-*b*-

https://doi.org/10.1021/acs.macromol.4c02808
Macromolecules 2025, 58, 4985−5000

PMMA (Figure 9a, b) and PI-*b*-P4VP BCPs (Figure 9g, h) exhibited significantly narrower morphological windows (Figure 1). Besides, when increasing the content of the incorporated homopolymer in the HICA process of the AB_m/B_n system, the degree of morphological transformation to higher-order structures followed the order: PI-*b*-PS_m/PS_n > PI-*b*-$PMMA_m/PMMA_n$ > PI-*b*-$P4VP_m/P4VP_n$. These differences might be related to two factors, namely, T_{sg} and the degree of solvation or plasticization of the core-forming block. On the one hand, the T_{sg} of PI-*b*-PMMA (68 °C) and PI-*b*-P4VP (The T_{sg} surpassed the temperature range from −60 to 75 °C set in the DSC program. By making an indirect inference from the T_g of the P4VP block, which is 132 °C, the T_{sg} of the P4VP block is definitely higher than that of PMMA and PS) was much higher than that of PI-*b*-PS (16 °C) (Figure S12b). As a result, at 90 °C in *n*-heptane, the solvophobic PMMA or P4VP block underwent much less solvation or plasticization. Therefore, during self-assembly, the core-forming volume (v) for the PMMA or P4VP block was lower, and the packing parameter (P) was smaller. On the other hand, compared to PMMA and PS, the P4VP block exhibited a significantly lower degree of solvation or plasticization in *n*-heptane, as supported by solubility parameters. Both PS (18.6 $MPa^{1/2}$) and PMMA (18.7 $MPa^{1/2}$) had solubility parameters lower than that of P4VP (23.0 $MPa^{1/2}$) and closer to that of *n*-heptane (15.3 $MPa^{1/2}$).[65−67] Consequently, by combining both T_{sg} and plasticization behavior, the mobility and rearrangement ability of the core-forming block in *n*-heptane followed the order PS > PMMA > P4VP, which aligned with the aforementioned findings in the self-assembly process. Additionally, based on the DSC analysis, the morphological transformation tendency to the higher-order region in the HICA process of the AB_m/AC_n system can also be explained (Figure 10). As the PMMA and P4VP blocks have relatively high T_{sg} and low degrees of solvation or plasticization in *n*-heptane, adding PI-*b*-PMMA or PI-*b*-P4VP to PI-*b*-PS was equivalent to adding a PS homopolymer or PI-*b*-PS with a higher PS content. This ultimately led to a transformation from spheres to worm-like morphologies. Especially in the PI_{77}-*b*-$P4VP_{50}/PI_{82}$-*b*-PS_{183} system (Figure 10h), a small number of spheres accompanied the worms, which differed from the complete formation of worms in the PI_{85}-*b*-$PMMA_{134}/PI_{82}$-*b*-PS_{183} system (Figure 10f). The reason may be attributed to the limited solvation degree of PI-*b*-P4VP BCP. Undoubtedly, it is believed that using an alternative solvent to enhance the solvation of 4VP would result in more abundant morphologies. However, related work is beyond the scope of this study and will be presented in future work.

CONCLUSIONS

In summary, the HISA process of PI-*b*-PS, PI-*b*-PMMA, and PI-*b*-P4VP was successfully exploited with a solids content of 20% w/w in *n*-heptane. Under identical conditions, the HICA process of AB_m/B_n (PI-*b*-PS_m/PS_n), AC_m/C_n (PI-*b*-$PMMA_m$/$PMMA_n$ and PI-*b*-$P4VP_m/P4VP_n$), AB_m/AB_n (PI-*b*-PS_m/PI-*b*-PS_n), and AB_m/AC_n (PI-*b*-PS_m/PI-*b*-$PMMA_n$ and PI-*b*-PS_m/PI-*b*-$P4VP_n$) systems was also achieved. The HISA and HICA processes produced nano-objects with a wide range of morphologies, including spheres, worms, vesicles, nanotubes, and sponges. Unlike the kinetically trapped morphologies in the PISA process, the morphologies generated in the HISA process represented a thermodynamic equilibrium state. With these results, the universality of HISA and HICA processes was sufficiently confirmed. The pseudophase diagrams of AB_m/B_n and AB_m/AB_n systems were constructed to elucidate the possible self-assembly mechanism and offer valuable principles for tailoring specific morphologies. The HISA and HICA techniques greatly broaden the scope of self-assembly and also bridge the gap between simple self-assembly and the formation of sophisticated morphologies. Especially, with the **high solids** content and ease of operation, the HISA and HICA techniques presented in this contribution hold significant potential for practical applications.

ASSOCIATED CONTENT

Supporting Information

. The Supporting Information is available free of charge at https://pubs.acs.org/doi/10.1021/acs.macromol.4c02808.

Experimental details and additional characterization data (PDF)

AUTHOR INFORMATION

Corresponding Author

Guowei Wang − *State Key Laboratory of Molecular Engineering of Polymers, Department of Macromolecular Science, Fudan University, Shanghai 200433, China;* orcid.org/0000-0003-2595-8269; Email: gwwang@fudan.edu.cn

Authors

Jingwei Zhang − *State Key Laboratory of Molecular Engineering of Polymers, Department of Macromolecular Science, Fudan University, Shanghai 200433, China*

Boyang Shi − *State Key Laboratory of Molecular Engineering of Polymers, Department of Macromolecular Science, Fudan University, Shanghai 200433, China*

Xiaoxiao Wu − *State Key Laboratory of Molecular Engineering of Polymers, Department of Macromolecular Science, Fudan University, Shanghai 200433, China*

Xiaotong Fang − *State Key Laboratory of Molecular Engineering of Polymers, Department of Macromolecular Science, Fudan University, Shanghai 200433, China*

Xinyue Liang − *State Key Laboratory of Molecular Engineering of Polymers, Department of Macromolecular Science, Fudan University, Shanghai 200433, China*

Zhou Peng − *State Key Laboratory of Molecular Engineering of Polymers, Department of Macromolecular Science, Fudan University, Shanghai 200433, China*

Complete contact information is available at: https://pubs.acs.org/10.1021/acs.macromol.4c02808

Notes

The authors declare no competing financial interest.

ACKNOWLEDGMENTS

This work is supported by the National Natural Science Foundation of China (22271058).

REFERENCES

(1) Blanazs, A.; Armes, S. P.; Ryan, A. J. Self-Assembled Block Copolymer Aggregates: From Micelles to Vesicles and their Biological Applications. *Macromol. Rapid Commun.* **2009**, *30*, 267−277.

(2) Zeng, Z.; Li, Z.; Li, Q.; Song, G.; Huo, M. Strong and Tough Nanostructured Hydrogels and Organogels Prepared by Polymerization-Induced Self-Assembly. *Small Methods* **2023**, *7*, No. e2201592.

(3) Holder, S. J.; Sommerdijk, N. New micellar morphologies from amphiphilic block copolymers: disks, toroids and bicontinuous micelles. *Polym. Chem.* **2011**, *2*, 1018−1028.
(4) Rodriguez-Hernandez, J.; Checot, F.; Gnanou, Y.; Lecommandoux, S. Toward 'smart' nano-objects by self-assembly of block copolymers in solution. *Prog. Polym. Sci.* **2005**, *30*, 691−724.
(5) Tritschler, U.; Pearce, S.; Gwyther, J.; Whittell, G. R.; Manners, I. 50th Anniversary Perspective: Functional Nanoparticles from the Solution Self-Assembly of Block Copolymers. *Macromolecules* **2017**, *50*, 3439−3463.
(6) Mai, Y.; Eisenberg, A. Self-assembly of block copolymers. *Chem. Soc. Rev.* **2012**, *41*, 5969−5985.
(7) Charleux, B.; Delaittre, G.; Rieger, J.; D'Agosto, F. Polymerization-Induced Self-Assembly: From Soluble Macromolecules to Block Copolymer Nano-Objects in One Step. *Macromolecules* **2012**, *45*, 6753−6765.
(8) Wang, X.; An, Z. New Insights into RAFT Dispersion Polymerization-Induced Self-Assembly: From Monomer Library, Morphological Control, and Stability to Driving Forces. *Macromol. Rapid Commun.* **2019**, *40*, 1800325.
(9) Penfold, N. J. W.; Yeow, J.; Boyer, C.; Armes, S. P. Emerging Trends in Polymerization-Induced Self-Assembly. *ACS Macro Lett.* **2019**, *8*, 1029−1054.
(10) Canning, S. L.; Smith, G. N.; Armes, S. P. A Critical Appraisal of RAFT-Mediated Polymerization-Induced Self Assembly. *Macromolecules* **2016**, *49*, 1985−2001.
(11) D'Agosto, F.; Rieger, J.; Lansalot, M. RAFT-Mediated Polymerization-Induced Self-Assembly. *Angew. Chem., Int. Ed.* **2020**, *59*, 8368−8392.
(12) Cornel, E. J.; Jiang, J.; Chen, S.; Du, J. Principles and Characteristics of Polymerization-Induced Self-Assembly with Various Polymerization Techniques. *CCS Chem.* **2021**, *3*, 2104−2125.
(13) Qiao, X. G.; Dugas, P. Y.; Charleux, B.; Lansalot, M.; Bourgeat-Lami, E. Synthesis of Multipod-like Silica/Polymer Latex Particles via Nitroxide-Mediated Polymerization-Induced Self-Assembly of Amphiphilic Block Copolymers. *Macromolecules* **2015**, *48*, 545−556.
(14) Groison, E.; Brusseau, S.; D'Agosto, F.; Magnet, S.; Inoubli, R.; Couvreur, L.; Charleux, B. Well-Defined Amphiphilic Block Copolymer Nanoobjects via Nitroxide-Mediated Emulsion Polymerization. *ACS Macro Lett.* **2012**, *1*, 47−51.
(15) Delaittre, G.; Dire, C.; Rieger, J.; Putaux, J. L.; Charleux, B. Formation of polymer vesicles by simultaneous chain growth and self-assembly of amphiphilic block copolymers. *Chem. Commun.* **2009**, 2887−2889.
(16) Derry, M. J.; Fielding, L. A.; Armes, S. P. Polymerization-induced self-assembly of block copolymer nanoparticles via RAFT non-aqueous dispersion polymerization. *Prog. Polym. Sci.* **2016**, *52*, 1−18.
(17) Warren, N. J.; Armes, S. P. Polymerization-Induced Self-Assembly of Block Copolymer Nano-objects via RAFT Aqueous Dispersion Polymerization. *J. Am. Chem. Soc.* **2014**, *136*, 10174−10185.
(18) Wang, X.; An, Z. S. New Insights into RAFT Dispersion Polymerization-Induced Self-Assembly: From Monomer Library, Morphological Control, and Stability to Driving Forces. *Macromol. Rapid Commun.* **2019**, *40*, 1800325.
(19) Wang, G.; Schmitt, M.; Wang, Z. Y.; Lee, B.; Pan, X. C.; Fu, L. Y.; Yan, J. J.; Li, S. P.; Xie, G. J.; Bockstaller, M. R.; et al. Polymerization-Induced Self-Assembly (PISA) Using ICAR ATRP at Low Catalyst Concentration. *Macromolecules* **2016**, *49*, 8605−8615.
(20) Wang, K.; Wang, Y. X.; Zhang, W. Q. Synthesis of diblock copolymer nano-assemblies by PISA under dispersion polymerization: comparison between ATRP and RAFT. *Polym. Chem.* **2017**, *8*, 6407−6415.
(21) Qu, S. W.; Wang, K.; Khan, H.; Xiong, W. F.; Zhang, W. Q. Synthesis of block copolymer nano-assemblies via ICAR ATRP and RAFT dispersion polymerization: how ATRP and RAFT lead to differences. *Polym. Chem.* **2019**, *10*, 1150−1157.
(22) Yoon, K. Y.; Lee, I. H.; Kim, K. O.; Jang, J.; Lee, E.; Choi, T. L. One-Pot in Situ Fabrication of Stable Nanocaterpillars Directly from Polyacetylene Diblock Copolymers Synthesized by Mild Ring-Opening Metathesis Polymerization. *J. Am. Chem. Soc.* **2012**, *134*, 14291−14294.
(23) Varlas, S.; Foster, J. C.; Arkinstall, L. A.; Jones, J. R.; Keogh, R.; Mathers, R. T.; O'Reilly, R. K. Predicting Monomers for Use in Aqueous Ring-Opening Metathesis Polymerization-Induced Self-Assembly. *ACS Macro Lett.* **2019**, *8*, 466−472.
(24) Le, D.; Dilger, M.; Pertici, V.; Diabate, S.; Gigmes, D.; Weiss, C.; Delaittre, G. Ultra-Fast Synthesis of Multivalent Radical Nanoparticles by Ring-Opening Metathesis Polymerization-Induced Self-Assembly. *Angew. Chem., Int. Ed.* **2019**, *58*, 4725−4731.
(25) Wang, J.; Cao, M.; Zhou, P.; Wang, G. Exploration of a Living Anionic Polymerization Mechanism into Polymerization-Induced Self-Assembly and Site-Specific Stabilization of the Formed Nano-Objects. *Macromolecules* **2020**, *53*, 3157−3165.
(26) Zhang, J.; Zhou, P.; Shi, B.; Li, P.; Wang, G. High-Efficient Access to Inverse Morphologies via Living Anionic Polymerization-Mediated Polymerization-Induced Cooperative Assembly. *Macromolecules* **2023**, *56*, 5743−5753.
(27) Yamauchi, K.; Hasegawa, H.; Hashimoto, T.; Tanaka, H.; Motokawa, R.; Koizumi, S. Direct Observation of Polymerization-Reaction-Induced Molecular Self-Assembling Process: In-Situ and Real-Time SANS Measurements during Living Anionic Polymerization of Polyisoprene-block-polystyrene. *Macromolecules* **2006**, *39*, 4531−4539.
(28) Zhu, A.; Lv, X.; Shen, L.; Zhang, B.; An, Z. Polymerization-Induced Cooperative Assembly of Block Copolymer and Homopolymer via RAFT Dispersion Polymerization. *ACS Macro Lett.* **2017**, *6*, 304−309.
(29) Tan, J.; Xu, Q.; Zhang, Y.; Huang, C.; Li, X.; He, J.; Zhang, L. Room Temperature Synthesis of Self-Assembled AB/B and ABC/BC Blends by Photoinitiated Polymerization-Induced Self-Assembly (Photo-PISA) in Water. *Macromolecules* **2018**, *51*, 7396−7406.
(30) Zhang, Y.; Han, G.; Cao, M.; Guo, T.; Zhang, W. Influence of Solvophilic Homopolymers on RAFT Polymerization-Induced Self-Assembly. *Macromolecules* **2018**, *51*, 4397−4406.
(31) Lv, F.; An, Z.; Wu, P. Efficient Access to Inverse Bicontinuous Mesophases via Polymerization-Induced Cooperative Assembly. *CCS Chem.* **2021**, *3*, 2211−2222.
(32) Byard, S. J.; O'Brien, C. T.; Derry, M. J.; Williams, M.; Mykhaylyk, O. O.; Blanazs, A.; Armes, S. P. Unique aqueous self-assembly behavior of a thermoresponsive diblock copolymer. *Chem. Sci.* **2020**, *11*, 396−402.
(33) Neal, T. J.; Penfold, N. J. W.; Armes, S. P. Reverse Sequence Polymerization-Induced Self-Assembly in Aqueous Media. *Angew. Chem., Int. Ed.* **2022**, *61*, No. e202207376.
(34) Penfold, N. J. W.; Neal, T. J.; Plait, C.; Leigh, A. E.; Chimonides, G.; Smallridge, M. J.; Armes, S. P. Reverse sequence polymerization-induced self-assembly in aqueous media: a counter-intuitive approach to sterically-stabilized diblock copolymer nano-objects. *Polym. Chem.* **2022**, *13*, 5980−5992.
(35) Farmer, M. A. H.; Musa, O. M.; Armes, S. P. Efficient Synthesis of Hydrolytically Degradable Block Copolymer Nanoparticles via Reverse Sequence Polymerization-Induced Self-Assembly in Aqueous Media. *Angew. Chem., Int. Ed.* **2023**, *62*, No. e202309526.
(36) Farmer, M. A. H.; Musa, O. M.; Armes, S. P. Combining Crystallization-Driven Self-Assembly with Reverse Sequence Polymerization-Induced Self-Assembly Enables the Efficient Synthesis of Hydrolytically Degradable Anisotropic Block Copolymer Nano-objects Directly in Concentrated Aqueous Media. *J. Am. Chem. Soc.* **2024**, *146*, 16926−16934.
(37) Farmer, M. A. H.; Musa, O. M.; Haug, I.; Naumann, S.; Armes, S. P. Synthesis of Poly(propylene oxide)-Poly(N,N'-dimethylacrylamide) Diblock Copolymer Nanoparticles via Reverse Sequence Polymerization-Induced Self-Assembly in Aqueous Solution. *Macromolecules* **2024**, *57*, 317−327.

https://doi.org/10.1021/acs.macromol.4c02808
Macromolecules 2025, 58, 4985−5000

(38) Kocik, M. K.; Mykhaylyk, O. O.; Armes, S. P. Aqueous worm gels can be reconstituted from freeze-dried diblock copolymer powder. *Soft Matter* **2014**, *10*, 3984−3992.
(39) Blanazs, A.; Verber, R.; Mykhaylyk, O. O.; Ryan, A. J.; Heath, J. Z.; Douglas, C. W.; Armes, S. P. Sterilizable gels from thermoresponsive block copolymer worms. *J. Am. Chem. Soc.* **2012**, *134*, 9741−9748.
(40) Fielding, L. A.; Lane, J. A.; Derry, M. J.; Mykhaylyk, O. O.; Armes, S. P. Thermo-responsive Diblock Copolymer Worm Gels in Non-polar Solvents. *J. Am. Chem. Soc.* **2014**, *136*, 5790−5798.
(41) Gu, Q.; Li, H.; Cornel, E. J.; Du, J. New driving forces and recent advances in polymerization-induced self-assembly. *Cell Rep. Phys. Sci.* **2023**, *4*, 101495.
(42) Wan, J.; Fan, B.; Thang, S. H. RAFT-mediated polymerization-induced self-assembly (RAFT-PISA): current status and future directions. *Chem. Sci.* **2022**, *13*, 4192−4224.
(43) Wang, G.; Wang, Z.; Lee, B.; Yuan, R.; Lu, Z.; Yan, J.; Pan, X.; Song, Y.; Bockstaller, M. R.; Matyjaszewski, K. Polymerization-induced self-assembly of acrylonitrile via ICAR ATRP. *Polymer* **2017**, *129*, 57−67.
(44) Petrov, A.; Chertovich, A. V.; Gavrilov, A. A. Phase Diagrams of Polymerization-Induced Self-Assembly Are Largely Determined by Polymer Recombination. *Polymers* **2022**, *14*, 5331.
(45) Li, Q.; He, X.; Cui, Y.; Shi, P.; Li, S.; Zhang, W. Doubly thermo-responsive nanoparticles constructed with two diblock copolymers prepared through the two macro-RAFT agents co-mediated dispersion RAFT polymerization. *Polym. Chem.* **2015**, *6*, 70−78.
(46) Ding, Z.; Gao, C.; Wang, S.; Liu, H.; Zhang, W. Macro-RAFT agent mediated dispersion polymerization: the monomer concentration effect on the morphology of the in situ synthesized block copolymer nano-objects. *Polym. Chem.* **2015**, *6*, 8003−8011.
(47) Wan, J.; Fan, B.; Putera, K.; Kim, J.; Banaszak Holl, M. M.; Thang, S. H. Polymerization-Induced Hierarchical Self-Assembly: From Monomer to Complex Colloidal Molecules and Beyond. *ACS Nano* **2021**, *15*, 13721−13731.
(48) Huo, M.; Zeng, M.; Li, D.; Liu, L.; Wei, Y.; Yuan, J. Tailoring the Multicompartment Nanostructures of Fluoro-Containing ABC Triblock Terpolymer Assemblies via Polymerization-Induced Self-Assembly. *Macromolecules* **2017**, *50*, 8212−8220.
(49) Niskanen, J.; Tenhu, H. How to manipulate the upper critical solution temperature (UCST)? *Polym. Chem.* **2017**, *8*, 220−232.
(50) Zhao, C.; Ma, Z.; Zhu, X. X. Rational design of thermoresponsive polymers in aqueous solutions: A thermodynamics map. *Prog. Polym. Sci.* **2019**, *90*, 269−291.
(51) Nan, Y.; Zhao, C.; Beaudoin, G.; Zhu, X. X. Synergistic Approaches in the Design and Applications of UCST Polymers. *Macromol. Rapid Commun.* **2023**, *44*, No. e2300261.
(52) Stejskal, J.; Hlavatá, D.; Sikora, A.; Konňák, C.ˇ.; Pleštil, J.; Kratochvíl, P. Equilibrium and non-equilibrium copolymer micelles: polystyrene-block-poly (ethylene-co-propylene) in decane and in diisopropylether. *Polymer* **1992**, *33*, 3675−3685.
(53) Hlavatá, D.; Stejskal, J.; Pleštil, J.; Koňák, C.ˇ.; Kratochvíl, P.; Helmstedt, M.; Mio, H.; Laggner, P. Heat-induced transition of polystyrene- block-poly(ethylene-co-propylene) micelles in decane and in dioxane. *Polymer* **1996**, *37*, 799−805.
(54) Growney, D. J.; Mykhaylyk, O. O.; Armes, S. P. Micellization and adsorption behavior of a near-monodisperse polystyrene-based diblock copolymer in nonpolar media. *Langmuir* **2014**, *30*, 6047−6056.
(55) Yuan, B.; He, X.; Qu, Y.; Gao, C.; Eiser, E.; Zhang, W. In situ synthesis of a self-assembled AB/B blend of poly(ethylene glycol)-b-polystyrene/polystyrene by dispersion RAFT polymerization. *Polym. Chem.* **2017**, *8*, 2173−2181.
(56) Tan, J.; Huang, C.; Liu, D.; Li, X.; He, J.; Xu, Q.; Zhang, L. Polymerization-Induced Self-Assembly of Homopolymer and Diblock Copolymer: A Facile Approach for Preparing Polymer Nano-Objects with Higher-Order Morphologies. *ACS Macro Lett.* **2017**, *6*, 298−303.
(57) Huang, C.; Tan, J.; Xu, Q.; He, J.; Li, X.; Liu, D.; Zhang, L. Adding a solvophilic comonomer to the polymerization-induced self-assembly of block copolymer and homopolymer: a cooperative strategy for preparing large compound vesicles. *RSC Adv.* **2017**, *7*, 46069−46081.
(58) Day, D. M.; Hutchings, L. R. The self-assembly and thermoresponsivity of poly(isoprene-b-methyl methacrylate) copolymers in non-polar solvents. *Eur. Polym. J.* **2021**, *156*, 110631.
(59) Obeng, M.; Milani, A. H.; Musa, M. S.; Cui, Z.; Fielding, L. A.; Farrand, L.; Goulding, M.; Saunders, B. R. Self-assembly of poly(lauryl methacrylate)-b-poly(benzyl methacrylate) nano-objects synthesised by ATRP and their temperature-responsive dispersion properties. *Soft Matter* **2017**, *13*, 2228−2238.
(60) O'Reilly, R. K.; Hawker, C. J.; Wooley, K. L. Cross-linked block copolymer micelles: functional nanostructures of great potential and versatility. *Chem. Soc. Rev.* **2006**, *35*, 1068−1083.
(61) Israelachvili, J. N. *Intermolecular and Surface Forces*, 3rd ed.; Elsevier: Amesterdam, 2011; pp 536−576. rd ed..
(62) Zhang, L. F.; Yu, K.; Eisenberg, A. Ion-induced morphological changes in "crew-cut" aggregates of amphiphilic block copolymers. *Science* **1996**, *272*, 1777−1779.
(63) Zhang, L. F.; Eisenberg, A. Morphogenic effect of added ions on crew-cut aggregates of polystyrene-b-poly(acrylic acid) block copolymers in solutions. *Macromolecules* **1996**, *29*, 8805−8815.
(64) Lu, H.; Song, W. Y.; Zou, Y. Y.; Xu, W. S.; Yan, Y. D.; Liu, H.; Ma, L. J. Kinetics and morphologies in polymerization-induced cooperative assembly: a computer simulation investigation. *Polym. Int.* **2022**, *71*, 359−365.
(65) Liu, H.; Gao, C.; Ding, Z.; Zhang, W. Synthesis of Polystyrene-block-Poly(4-vinylpyridine) Ellipsoids through Macro-RAFT-Agent-Mediated Dispersion Polymerization: The Solvent Effect on the Morphology of the In Situ Synthesized Block Copolymer Nano-objects. *Macromol. Chem. Phys.* **2016**, *217*, 467−476.
(66) Cong, Y.; Zhang, Z.; Fu, J.; Li, J.; Han, Y. Water-induced morphology evolution of block copolymer micellar thin films. *Polymer* **2005**, *46*, 5377−5384.
(67) Park, S.-Y.; Sul, W.-H.; Chang, Y.-J. A Study on the Selectivity of Toluene/Ethanol Mixtures on the Micellar and Ordered Structures of Poly(styrene-b-4-vinylpyridine) Using Small-angle X-ray Scattering, Generalized Indirect Fourier Transform, and Transmission Electron Microscopy. *Macromolecules* **2007**, *40*, 3757−3764.

https://doi.org/10.1021/acs.macromol.4c02808
Macromolecules 2025, 58, 4985−5000